

# 28nm High-K Metal Gate RF CMOS TCAD Calibration

by

Jiabi Zhang

A thesis submitted to the Graduate Faculty of  
Auburn University  
in partial fulfillment of the  
requirements for the Degree of  
Master of Science

Auburn, Alabama  
December 12, 2015

Keywords: *28nm*, CMOS, Noise

Copyright 2015 by Jiabi Zhang

Approved by

Guofu Niu, Professor of Electrical and Computer Engineering  
Foster Dai, Professor of Electrical and Computer Engineering  
Michael Hamilton, Professor of Electrical and Computer Engineering

## Abstract

States of art of  $28nm$  MOSFET structure is studied using the calibrated simulation deck, RF noise is simulated and compared with measurements. DC characteristics is firstly calibrated by adjusting doping profiles and other physical models include mobility and energy relaxation time model parameters. For DC calibration, body effect is focused on. DIBL(Drain Induced Barrier Lowering)and SS(Subthreshold slope) are fitted by fitting simulation  $I_{DS} - V_{GS}$  curves and  $I_{DS} - V_{DS}$  curves to measurement data.

## Acknowledgments

I want to thank my parents. To thank them for giving me the great opportunity of studying abroad. I want to thank them for providing me with steady guidance and encouragement. Their love for me are the source of my braveness and strength. I would like to thank Dr. Guofu Niu, for his support and encouragement of my research. When I firstly came to Auburn and became a graduate student, I had very few semiconductor and transistor knowledge. At that time I don't even know what TCAD is. It is Dr. Niu that taught me step by step of how to use this software in his class, and gave me many ideas on my research projects. When I met problems in my research, Dr. Niu would give me his opinion and his opinions help a lot. I feel so lucky to have the opportunity to be the student of Dr. Niu and I am really grateful. I also want to thank Dr. Michael Hamilton and Dr. Fa Dai, who served on my master's thesis committee. I want to thank for their valuable comments and precious time. Their courses gave me a solid knowledge background for my research. I would like to express my sincere gratitude to former and current members in our research group. I want to thank Jingyi Wang for teaching me how to use TCAD and helping me with my master's work. I would like to thank Zhen Li for his patience answering all of my questions. I would like to thank Huaiyuan Zhang for his extraction data and his help in MATLAB programming. I would like to thank Rongchen Ma, for his advice and encouragement. I would like to thank Yili Wang, Pengyu Li and Yiao Li and all friends in Auburn.

## Table of Contents

|  |     |
|--|-----|
| Abstract . . . . .   | ii  |
| Acknowledgments . . . . .                                      | iii |
| List of Figures . . . . .                                      | vi  |
| List of Tables . . . . .                                       | x   |
| 1 Introduction . . . . .                                       | 1   |
| 1.1 MOSFET Noise Introduction . . . . .                        | 1   |
| 1.1.1 Thermal Noise in MOSFETs . . . . .                       | 2   |
| 1.1.2 Impedance Field Method Introduction . . . . .            | 4   |
| 1.2 Research Progress on Short Channel MOSFETs Noise . . . . . | 6   |
| 2 Device Structure . . . . .                                   | 9   |
| 2.1 Simulation Structure Development . . . . .                 | 10  |
| 2.2 Device Calibration . . . . .                               | 12  |
| 2.3 Capacitance Calibration . . . . .                          | 13  |
| 2.3.1 EOT calibration . . . . .                                | 13  |
| 2.3.2 Work function calibration . . . . .                      | 13  |
| 2.3.3 Capacitance Calibration Results . . . . .                | 14  |
| 2.4 $R_s$ and $R_d$ Calibration . . . . .                      | 16  |
| 2.5 DC I-V Calibration . . . . .                               | 17  |
| 2.5.1 DIBL and SS calibration . . . . .                        | 17  |
| 2.5.2 Body Effect calibration . . . . .                        | 22  |
| 2.6 Physics Model Calibration . . . . .                        | 34  |
| 2.6.1 Lombardi Mobility Model . . . . .                        | 35  |
| 2.6.2 Low field mobility calibration . . . . .                 | 37  |

|       |  |    |
|-------|--|----|
| 2.6.3 | High field mobility calibration . . . . .                  | 39 |
| 2.7   | Conclusion . . . . .                                       | 45 |
| 3     | Noise Simulation and Interpretation . . . . .              | 46 |
| 3.1   | TCAD noise simulation . . . . .                            | 46 |
| 3.2   | DD and HD Model for Noise simulation . . . . .             | 46 |
| 3.3   | Impedance Field Method in TCAD Simulation . . . . .        | 48 |
| 3.4   | Noise Simulation Result and Analysis . . . . .             | 54 |
| 3.5   | Noise simulation and measurement data comparison . . . . . | 56 |
| 4     | Conclusion and Future Work . . . . .                       | 58 |
|       | Bibliography . . . . .                                     | 59 |

## List of Figures

|     |  |    |
|-----|--|----|
| 1.1 | Illustration of gate current thermal noise and thermal noise in the channel, in MOSFETs[4]. . . . .                      | 3  |
| 1.2 | MOSFET noise model using gate noise current, drain noise currents, and their correlation[5]. . . . .                     | 4  |
| 1.3 | Impedance field method [6]. . . . .  | 5  |
| 1.4 | Noise parameter $\Gamma$ versus channel length[9]. . . . .   | 7  |
| 1.5 | Noise modelling versus channel length[11]. . . . .   | 8  |
| 2.1 | Calibration strategy. . . . .  | 9  |
| 2.2 | TCAD structure step by step development illustration. . . . .  | 11 |
| 2.3 | Simulated and calibrated 28nm gate length device structure. . . . .  | 12 |
| 2.4 | 28nm NMOS $C_{gg}$ calibration using calibrated EOT and metal gate work function. . . . .                                | 14 |
| 2.5 | 28nm NMOS $C_{gc}$ calibration using calibrated EOT and metal gate work function. . . . .                                | 15 |
| 2.6 | 28nm NMOS doping concentration along channel length. . . . .   | 15 |
| 2.7 | Source and drain resistance extraction. . . . .  | 17 |
| 2.8 | Band diagram of long channel and short channel MOSFET devices showing Drain Induced Barrier Lowering effect[15]. . . . . | 18 |

|      |   |    |
|------|---|----|
| 2.9  | Simulated band diagram of 28nm gate length device for Drain Induced Barrier Lowering effect illustration. . . . .         | 19 |
| 2.10 | DIBL and SS calculation illustration. . . . .   | 20 |
| 2.11 | Simulated $I_{DS} - V_{DS}$ curves before DIBL and SS calibration. . . . .  | 21 |
| 2.12 | Simulated $I_{DS} - V_{DS}$ curves when $V_{DS} = 0.05V$ , $V_{DS} = 0.4V$ , $V_{DS} = 0.75V$ , $V_{DS} = 1.0V$ . . . . . | 21 |
| 2.13 | DIBL and SS Calibration illustration. . . . .   | 22 |
| 2.14 | Body Effect Introduction[16]. . . . .   | 23 |
| 2.15 | Depletion layer change under different body bias. . . . .   | 24 |
| 2.16 | Substrate doping simulation illustration. . . . .   | 25 |
| 2.17 | Substrate doping impact on body effect. . . . .   | 26 |
| 2.18 | Halo doping peak concentration simulation. . . . .  | 27 |
| 2.19 | Halo peak concentration impact on body effect. . . . .  | 28 |
| 2.20 | Halo doping depth simulation. . . . .   | 29 |
| 2.21 | Halo depth impact on body effect. . . . .   | 29 |
| 2.22 | Channel doping simulation. . . . .  | 30 |
| 2.23 | Channel doping impact on body effect. . . . .   | 31 |
| 2.24 | Source and drain extension doping simulation. . . . .   | 32 |
| 2.25 | Source and drain extension doping impact on body effect. . . . .  | 32 |

|      |   |    |
|------|---|----|
| 2.26 | Source and drain extension doping simulation. . . . .   | 33 |
| 2.27 | Source and drain extension doping impact on body effect. . . . .  | 34 |
| 2.28 | $I_{DS} - V_{GS}$ curve fitting result for low field mobility parameter values under $V_{ds} = 0.05V$ . . . . .                                   | 38 |
| 2.29 | Calibrated $I_{DS} - V_{GS}$ curve illustration for low field mobility parameter values under $V_{ds} = 0.05V$ . . . . .                          | 39 |
| 2.30 | $I_{DS} - V_{GS}$ curve fitting result using calibrated mobility parameter values for both parameter combinations under $V_{DS} = 1.1V$ . . . . . | 41 |
| 2.31 | $I_{DS} - V_{GS}$ curve linear scale fitting result with $V_{GS}$ : $0.05V, 0.4V, 0.6V, 1.1V$ . . . . .   | 42 |
| 2.32 | $I_{DS} - V_{GS}$ curve log scale fitting result with $V_{GS}$ : $0.05V, 0.4V, 0.6V, 1.1V$ . . . . .  | 43 |
| 2.33 | $I_{DS} - V_{DS}$ curve linear scale fitting result with multiple biases using $\tau = 0.02ps$ , $V_{sat} = 1.2e7cm/s$ . . . . .                  | 43 |
| 2.34 | $I_{DS} - V_{DS}$ curve log scale fitting result with multiple biases using $\tau = 0.02ps$ , $V_{sat} = 1.2e7cm/s$ . . . . .                     | 44 |
| 2.35 | $I_{DS} - V_{DS}$ curve linear scale fitting result with multiple biases using $\tau = 0.007ps$ , $V_{sat} = 1.3e7cm/s$ . . . . .                 | 44 |
| 2.36 | $I_{DS} - V_{DS}$ curve log scale fitting result with multiple biases using $\tau = 0.007ps$ , $V_{sat} = 1.3e7cm/s$ . . . . .                    | 45 |
| 3.1  | Local noise source distribution in device at $f = 10GHz$ , $V_{DS} = 0.6V$ , $V_{GS} = 0.6V$ . . . . .  | 49 |
| 3.2  | Local noise source simulated cut data at $f = 10GHz$ , $V_{DS} = 0.6V$ , $V_{GS} = 0.6V$ . . . . .  | 50 |

|     |   |    |
|-----|---|----|
| 3.3 | Green function $f = 10GHz$ , $V_{DS} = 0.6V$ , $V_{GS} = 0.6V$ . . . . .  | 51 |
| 3.4 | Vctor Green's function simulated data at $f = 10GHz$ , $V_{DS} = 0.6V$ , $V_{GS} = 0.6V$ . . . . .                  | 52 |
| 3.5 | Local noise current spectral density distribution at $f = 10GHz$ , $V_{DS} = 0.6V$ ,<br>$V_{GS} = 0.6V$ . . . . .   | 53 |
| 3.6 | Local noise current spectral density simulated data at $f = 10GHz$ , $V_{DS} = 0.6V$ ,<br>$V_{GS} = 0.6V$ . . . . . | 54 |
| 3.7 | Simulated $\gamma_{gd_0}$ versus $V_{DS}$ at $V_{GS} = 0.3V$ . . . . .  | 55 |
| 3.8 | Simulated $\gamma_{gd_0}$ versus $V_{DS}$ at $V_{GS} = 0.5V$ . . . . .  | 55 |
| 3.9 | Noise simulation and measurement comparison $\tau = 0.02ps$ , $V_{sat} = 1.2 \times 10^7 cm/s$ . . . . .            | 57 |

## List of Tables

|     |   |    |
|-----|---|----|
| 2.1 | Constant mobility default coefficient. . . . .          | 35 |
| 2.2 | Doping dependent mobility default coefficients. . . . . | 36 |
| 2.3 | Lombardi mobility model default coefficient. . . . .    | 37 |
| 2.4 | Low field mobility model parameter calibration. . . . . | 38 |
| 2.5 | Velocity saturation parameters. . . . .                 | 40 |
| 2.6 | High field mobility parameter calibration. . . . .      | 40 |

## Chapter 1

### Introduction

As one of the most advanced transistor technologies, the  $28nm$  gate length MOSFET technology has been under research for a period of time. With the functionality of the transistors improve, the focus of developers has switched to its applications. RF circuits have so many applications in our daily life such as WI-Fi, bluetooth and GPS systems. The adoption of  $28nm$  MOSFETs to RF circuits is becoming more and more important. In order to do so, many side effects need to be considered. The subject of RF noise is of great importance, so RF noise has received extensive treatment in literatures. In this section an short introduction of MOSFETs noise will be given.

#### 1.1 MOSFET Noise Introduction

There are several types of device noise in MOSFETs: thermal noise, shot noise and flicker noise. Thermal noise, a well-known example of noise, is also called Johnson noise or Nyquist noise[1]. The mechanism of thermal noise is the random motion of carriers.

$$S_{vt} = 4kTR, \quad (1.1)$$

where  $S_{vt}$  is power spectral density of  $v_n$ ,  $k$  is Boltzmann's constant,  $T$  represents the absolute temperature, and  $R$  represents a an ideal (noiseless) resistor in a series with a noise voltage source. This method is usually used to calculate thermal noise for a given resistor. Shot noise is another normal noise type. This type of noise is associated dc flow produced by

carriers crossing a potential barrier and is due to the discreteness of arriving charges.

$$S_{is} = 2qI \quad (1.2)$$

where  $S_{is}$  is the power spectral density of  $i_n$ ,  $q$  is charge magnitude, and  $I$  is the current flow.  $v_n$  is voltage spectral density. In MOSFETs, thermal noise is the most common type and will be discussed.

### 1.1.1 Thermal Noise in MOSFETs

Figure 1.1 gives a brief illustration of the mechanism of thermal noise in MOSFETs. Thermal noise in MOSFETs is due to the fluctuation in the channel in surface potential. It is easy to see from Figure 1.1 that there are mainly 2 types of thermal noise: drain induced current and gate induced current noise. Noise power spectral density (PSD) of drain current noise and voltage current noise are correlated, and the correlation is imaginary due to the capacitive nature of gate to channel coupling. Van der Ziel [2] derived power spectral density of drain current noise and gate current noise for long channel MOSFETs devices.

$$S_{id} = \gamma_{gd0} \cdot 4kTg_{d0} \quad (1.3)$$

$$S_{ig} = \beta 4kTg_g \quad (1.4)$$

where  $S_{id}$  and  $S_{ig}$  are power spectral densities for drain and gate noise currents.  $k$  is Boltzmann's constant,  $gd0$  is the zero  $V_{DS}$  channel conductance,  $g_g$  is the gate conductance,  $\beta$  is the function of terminal bias.  $\gamma_{gd0}$  represents the noise parameter[3].

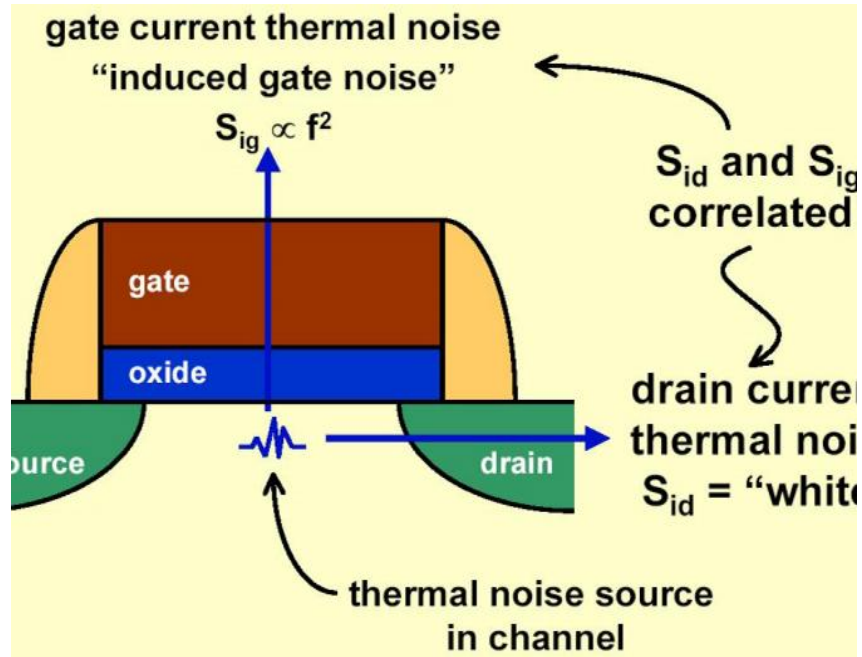


Figure 1.1: Illustration of gate current thermal noise and thermal noise in the channel, in MOSFETs[4].

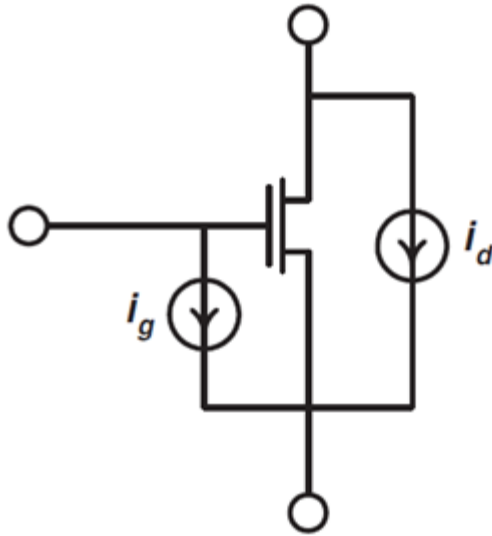


Figure 1.2: MOSFET noise model using gate noise current, drain noise currents, and their correlation[5].

### 1.1.2 Impedance Field Method Introduction

The thermal noise in MOSFETs can be calculated using impedance field method. Impedance field method is illustrated in Figure 1.3. In the device velocity fluctuation causes current density fluctuation. Current density fluctuation at each location propagate towards the contact and noise voltage fluctuation result at each contact assuming open circuit. Sentaurus Device also computes the variances and correlation coefficients of the currents through the nodes, assuming fixed voltages; these quantities are the noise current spectral densities. The first task is to provide models for the noise sources. Noise sources are defined as Local Noise Source (LNS) in TCAD sdevice simulator. Diffusion noise sources is used. Diffusion noise is due to the fluctuations of the velocities of the carriers, produced by the collisions with phonons, impurities. The second task is determining the impact of the local fluctuation on the terminal noise. Linear relationship is described by applying the Green functions.

$$C^r n_{s_i} = 4qnD_n \quad (1.5)$$

$$C^r p_{s_i} = 4qnD_p \quad (1.6)$$

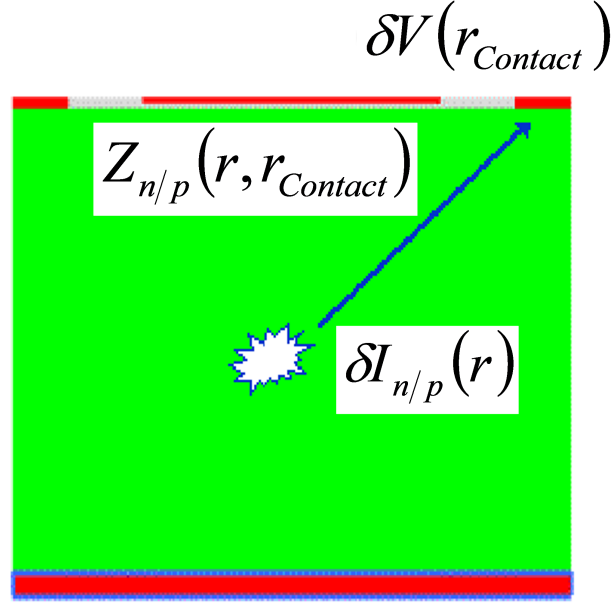


Figure 1.3: Impedance field method [6].

Furthermore, the local noise source  $C_{s_i}$  are proportional to carrier density and diffusivity, where superscripts  $n$  and  $p$  denote electron and hole respectively. In the equations,  $n$  represents electron concentration and  $p$  represents hole concentration,  $D_n$  and  $D_p$  represents the diffusivity of electrons and holes. The source unit is  $A^2/HZ/cm^3$ . The equation of calculating impedance field  $\tilde{Z}_n(r, r_{contact})$  can be derived as: [6]

$$\tilde{Z}_n(r, r_{contact}) = \frac{1}{q} \nabla_r Z_n(r, r_{contact}) \quad (1.7)$$

$$\tilde{Z}_p(r, r_{contact}) = \frac{1}{q} \nabla_r Z_p(r, r_{contact}) \quad (1.8)$$

where  $\tilde{Z}_n(r, r_{contact})$  and  $\tilde{Z}_p(r, r_{contact})$  are the impedance field from local noise source to terminal noise voltage. So we have  $|\tilde{Z}_n(r, r_{contact})|^2$  and  $\tilde{Z}_p(r, r_{contact})^2$  whose units are  $V^2/A^2$ . The terminal noise voltage power spectral density is obtained by integrating the noise concentration over the device volume.

## 1.2 Research Progress on Short Channel MOSFETs Noise

In the analytical formulations, they took into account effects like the field dependant noise temperature and mobility, the device geometry and the channel length modulation, the back gate effect and the velocity saturation. The noise parameter  $\gamma$  was introduced for noise analysis. The compact modelling of  $\gamma$  has been conducting for years. Figure 1.4 shows the research on the effect on channel noise. Hot-carrier effects are investigated after the theory of thermal noise. From standard theory, the noise parameter  $\gamma$  would have value unity and at  $V_{DS} = 0$  and monotonically decrease to a value  $2/3$  as the device approached saturation. However, Jindal found that  $\gamma$  actually increased steadily with increasing  $V_{DS}$ [7][8][10]. The initial rise instead of a decline in  $\gamma$  as a function of  $V_{DS}$  is believed to be due to carriers getting hotter[7]. The  $\gamma$  value results are illustrated in Fig 1.4. Figure 1.5 shows a recent noise modelling research. Noise parameter  $\gamma$  can be fitted for measurement data for MOSFETs from  $40nm$  to  $200nm$  gate length devices.  $28nm$  MOSFET devices are not included in the recent research which is a reason for me to to write this paper.



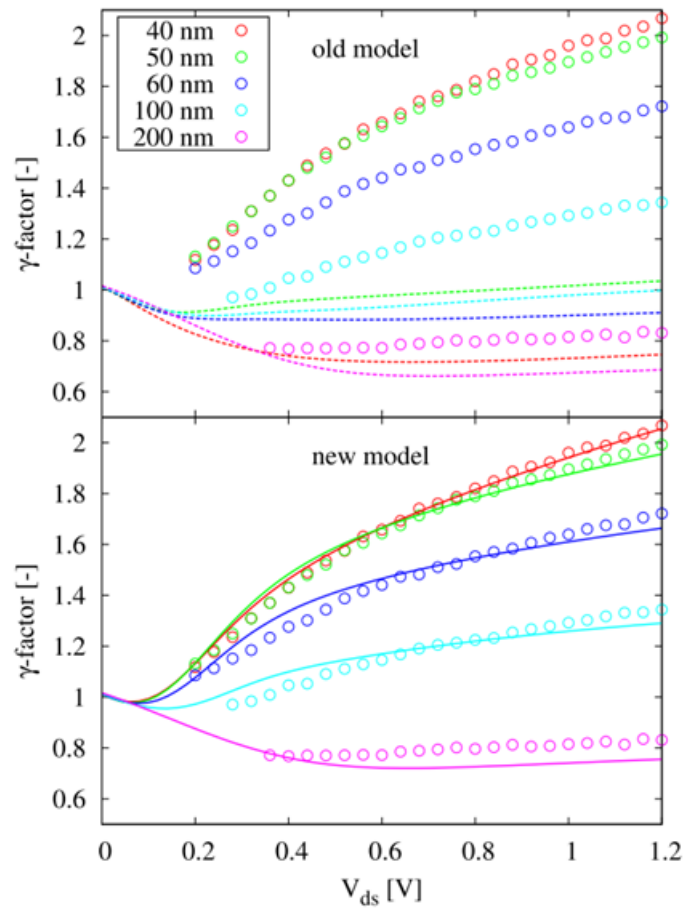


Figure 1.5: Noise modelling versus channel length[11].

Chapter 2  
Device Structure

This chapter gives a summary of the methodologies used in simulation structure construction. TCAD tool Sentaurus Device Editor(SDE) is used to build the device structure. Figure 2.1 illustrates the basic steps used in this research.

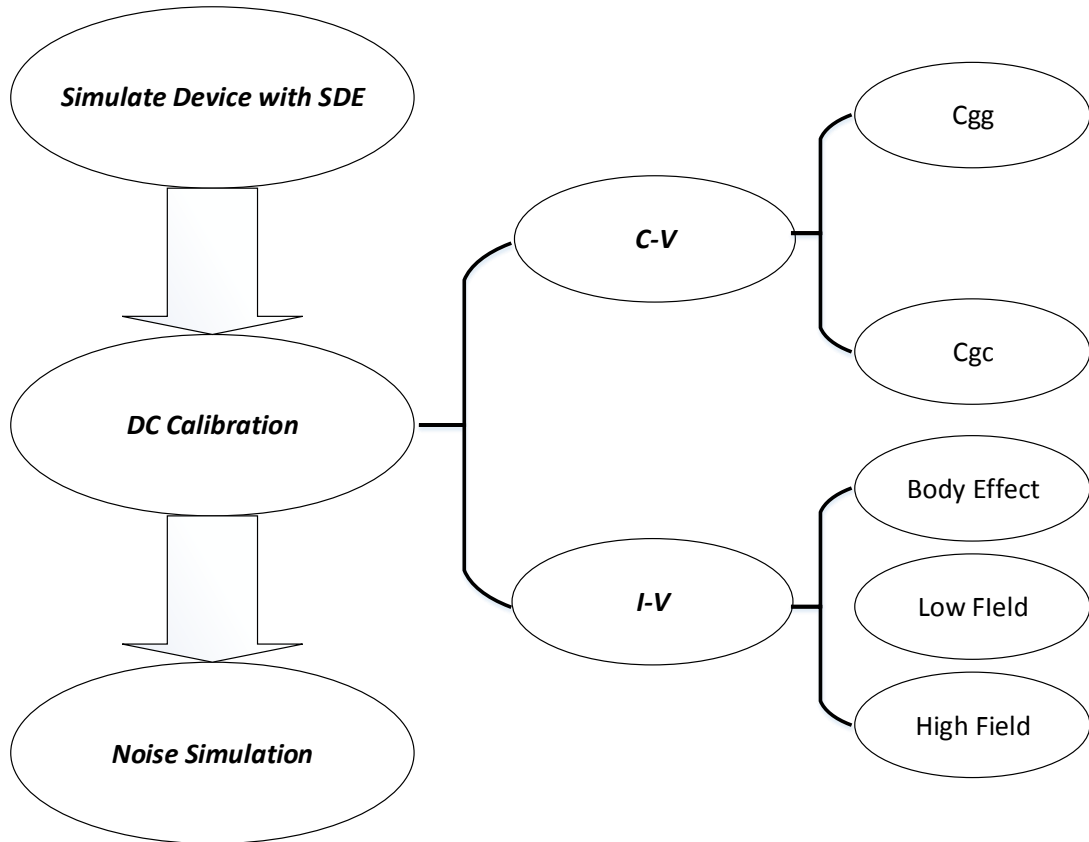


Figure 2.1: Calibration strategy.

Sentaurus Device Editor(SDE) is a tool for both 2-dimensional and 3-dimensional structure editing, which include geometric model generation, doping and refinement definition and

submesh inclusion[13]. Compared to other tools in TCAD, Sentaurus Device Editor provides much higher flexibility in doping profiles change and meshing strategies. A 2-dimensional 28nm High-K metal gate RF CMOS structure is simulated and calibrated.

## 2.1 Simulation Structure Development

In TCAD, several device construct methodologies are introduced, the most widely used are two methods: Sentaurus Process (sprocess). This simulator simulates process steps such as implantation, oxidation, etching, deposition, silicidation for both 2D and 3D structures[14]. The second method used a simulator called Sentaurus Structure Editor (SDE). Structures are generated or edited interactively using graphical user interfaces. Sprocess is more closer to actual fabrication processes while SDE is more flexible in doping profile and layout setup. Figure 2.3 shows the simulation structure of this research. The structure shown is a calibrated 28nm High-k metal gate, 2-dimensional n-type MOSFETs. On account of short channel effect for 28nm gate length devices, common oxide is replaced by High-K material (HfO<sub>2</sub>) and oxide for gate oxide. Besides, gate material is changed from poly-silicon to metal. High-K material is widely used in modern fabrication technologies, in order to control leakage after shrinking the thickness of insulator. For source and drain, two layers are created, the shallow n- LDD region overlaps with the gate area which helps in gate control. The second layer is an n+ region working as source and drain. Halo doping is also created. Both the source/drain doping and halo doping are created using Gaussian profile. These doping profiles are very important and they are adjusted in the calibration steps to fit the C-V and I-V measurement data. Figure 2.2 shows the basic steps of SDE simulation structure development.

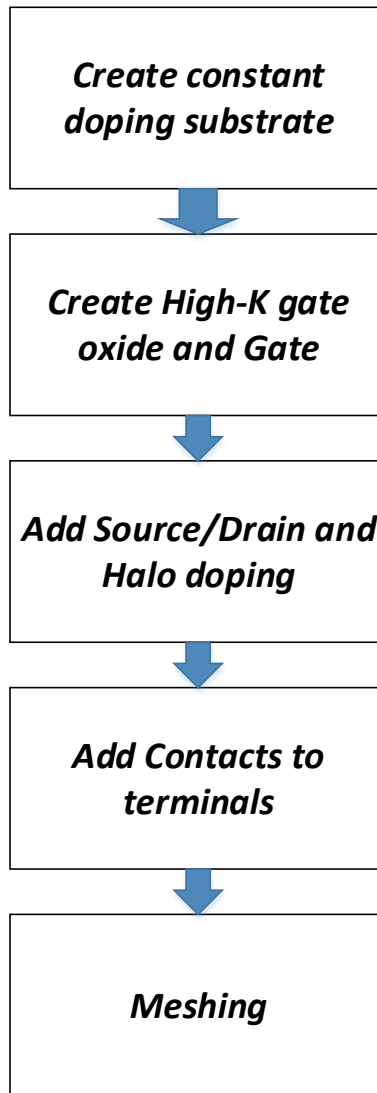


Figure 2.2: TCAD structure step by step development illustration.

Educated guess is applied in device structure construction. Figure 2.3 illustrates the calibrated 2D device which also shows the doping informations and meshing strategies. In the zoom in screen shot, meshing strategies can be seen: more mesh in channel region and source, drain region, less mesh in the substrate and gate region. Constant meshing is used in constant doped areas and multi-box meshing is used in analytical doping areas. Channel region has large influence on I-V characterizations so need to be heavily meshed.

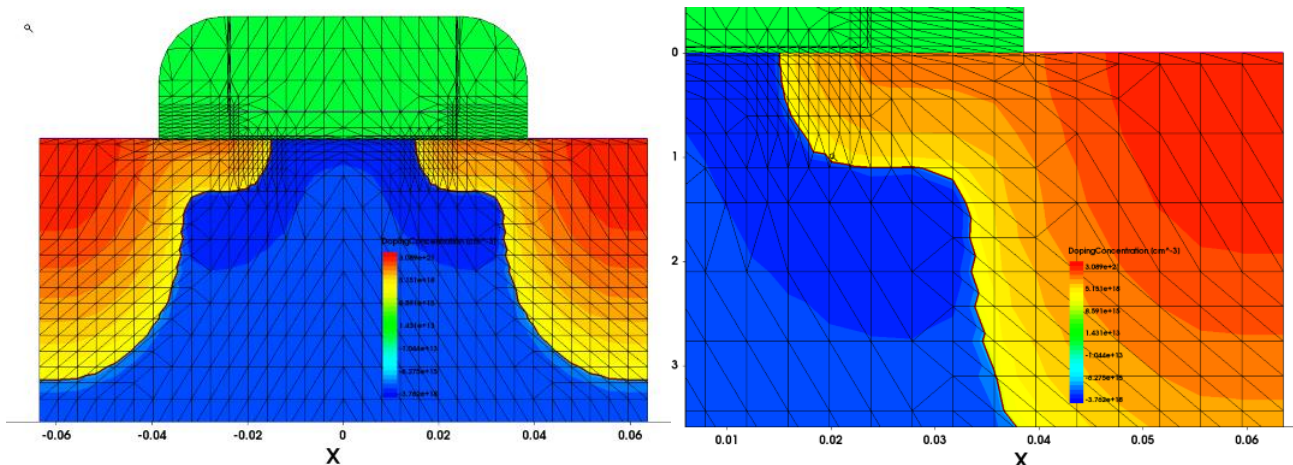


Figure 2.3: Simulated and calibrated 28nm gate length device structure.

## 2.2 Device Calibration

DC calibration has three separate sections: C-V calibration,  $R_s, R_d$  calibration and I-V calibration. Capacitance calibration is the first step for calibration since in MOSFETs devices, capacitance are mostly influenced by effective oxide thickness, work function of metal gate and doping profiles. Capacitance calibration is able to determine EOT work function and basic shape of doping profiles. Then I-V calibration is conduct because among the three calibration sections, I-V calibration is the most important step. In this step not only doping profiles, junction depth, short-channel effects can be calibrated, but also mobility model parameters. After I-V calibration section, simulation currents can fit the measurement data. I-V calibration include three parts: body effect calibration, low field calibration and high field calibration. Body effect calibration focus on DC I-V characteristic calibrations. Lombardi mobility model is used in low  $V_{DS}$  conditions. Low field mobility calibration is carried out first since in low field some high field parameter impact can be ignored such as: saturation velocity, energy relaxation time. After low field mobility model calibration, high field calibration is done. Source and drain resistance are mainly affected by source and drain doping.

## 2.3 Capacitance Calibration

Capacitance is not only influenced by the thickness of oxide and doping profiles. EOT calculation is the first step in capacitance calibration.

### 2.3.1 EOT calibration

$$EOT = \left( \frac{C}{Area} \cdot \frac{1}{\epsilon_{SiO_2}} \right)^{-1}, \quad (2.1)$$

where C is the strong inversion capacitance, Area is the area of the gate oxide,

$$Area = W \cdot L, \quad (2.2)$$

$$\epsilon = \epsilon_r \cdot \epsilon_0, \quad (2.3)$$

$$\frac{1}{C_{SiO_2}} + \frac{1}{C_{HfO_2}} = \frac{1}{C}, \quad (2.4)$$

where  $C_{SiO_2}$  and  $C_{HfO_2}$  are corresponding to the capacitance of  $SiO_2$  and capacitance of  $HfO_2$ . The measurement data of long channel devices with  $L = 10\mu m$ ,  $W = 10\mu m$  is applied in the EOT calibration. The reason for using a long channel and wide W device measurement data for calculation is to minimize the influence of parasitic capacitance. In long channel and devices the intrinsic capacitance is dominant while in short channel devices the parasitic capacitance can be comparable to intrinsic capacitances. After EOT calibration, thickness of high-k material and oxide need to be determined. Since fringing capacitance exists, simulated capacitance is larger than measurement data.

### 2.3.2 Work function calibration

Then after TCAD simulation, the simulated C-V curve and measurement C-V curve are compared and displayed in the same figure. By matching the two curves, the final thickness for High-k material and oxide are obtained. In the simulation device structure  $HfO_2$  material

is used.  $HfO_2$  is also a commonly used high-k material in fabrication industry. The work function is defined in Sentaurus device simulation script,

### 2.3.3 Capacitance Calibration Results

$C_{gg}$  and  $C_{gc}$  capacitance are investigated with calculated  $EOT = 1.448nm$ .  $C_{gg}$  is by definition as gate capacitance. In simulation, body, gate and S/D are all tied together and it is obtained by Y parameter analysis.  $C_{gc}$  is not the normally defined channel capacitance.  $C_{gc}$  equals to capacitance  $C_{gg}$  minus capacitance  $C_{gb}$ . Figure 2.4 and Figure 2.5 show the calibrated capacitances, and Figure 2.6 shows the doping profile along the channel after a lateral cut on the device.

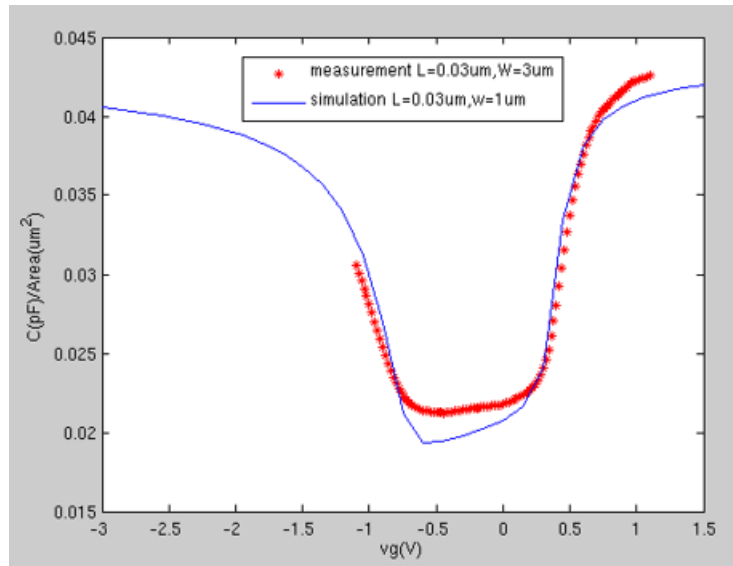


Figure 2.4: 28nm NMOS  $C_{gg}$  calibration using calibrated EOT and metal gate work function.

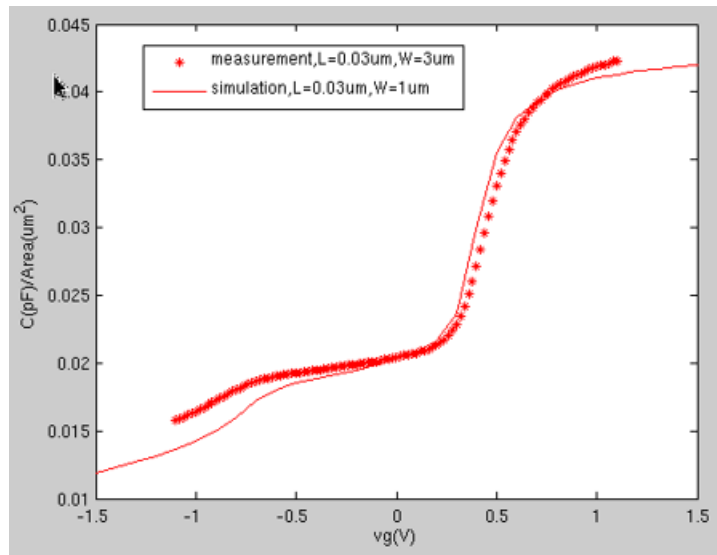


Figure 2.5: 28nm NMOS  $C_{gc}$  calibration using calibrated EOT and metal gate work function.

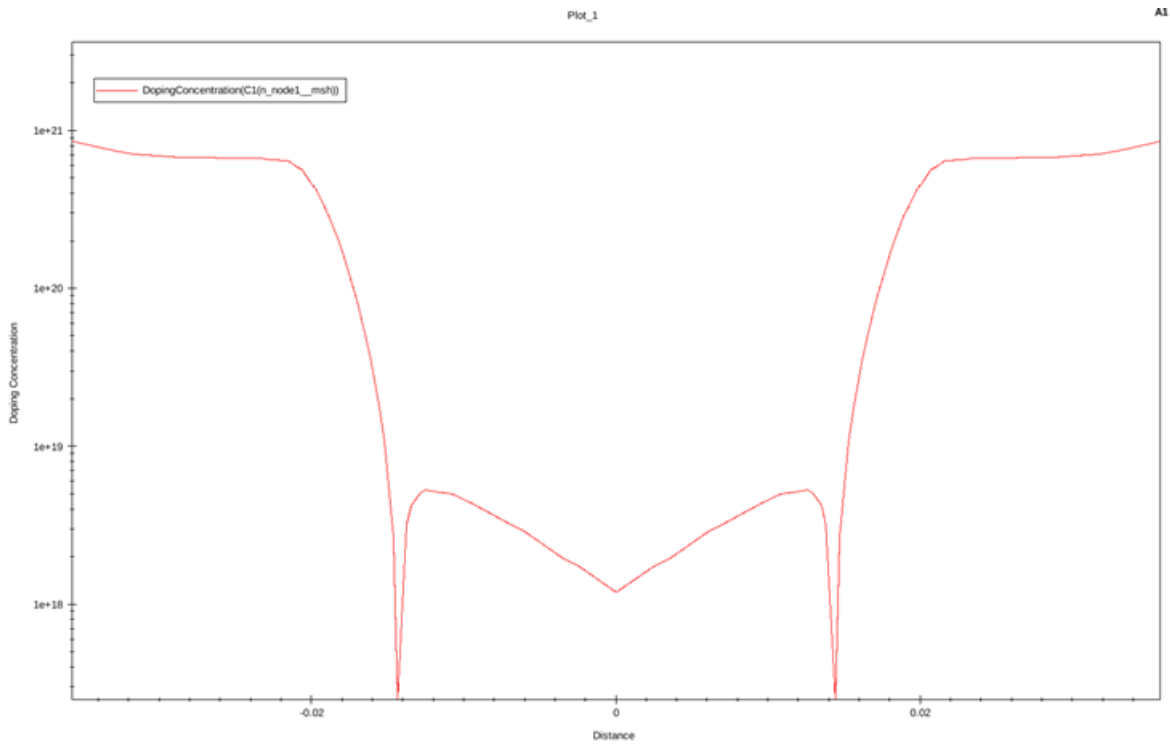


Figure 2.6: 28nm NMOS doping concentration along channel length.

## 2.4 $R_s$ and $R_d$ Calibration

Source and drain resistance are very important parameters which have mass impact on *DC* characteristics and thermal noise. So it is important to have source and drain resistance extracted and calibrated before noise simulation. In short-channel devices, source and drain resistance can be extracted by intercepting 2 curves.  $R_d$  is the interception of curve ( $Real[Z_{22} - Z_{12}]$ ) versus  $1/(V_{gs} - V_{th})$ ;  $R_s$  is the interception of curve  $Real[Z_{12}]$  versus  $1/(V_{gs} - V_{th})$ . From the measurement data, the extracted  $R_d$  and  $R_s$  are approximately  $80\Omega$ . So by changing source and drain doping profiles it is necessary to set source and drain resistance to  $80\Omega$ . Figure 2.7 shows the simulation result of the  $R_s$  and  $R_d$ .

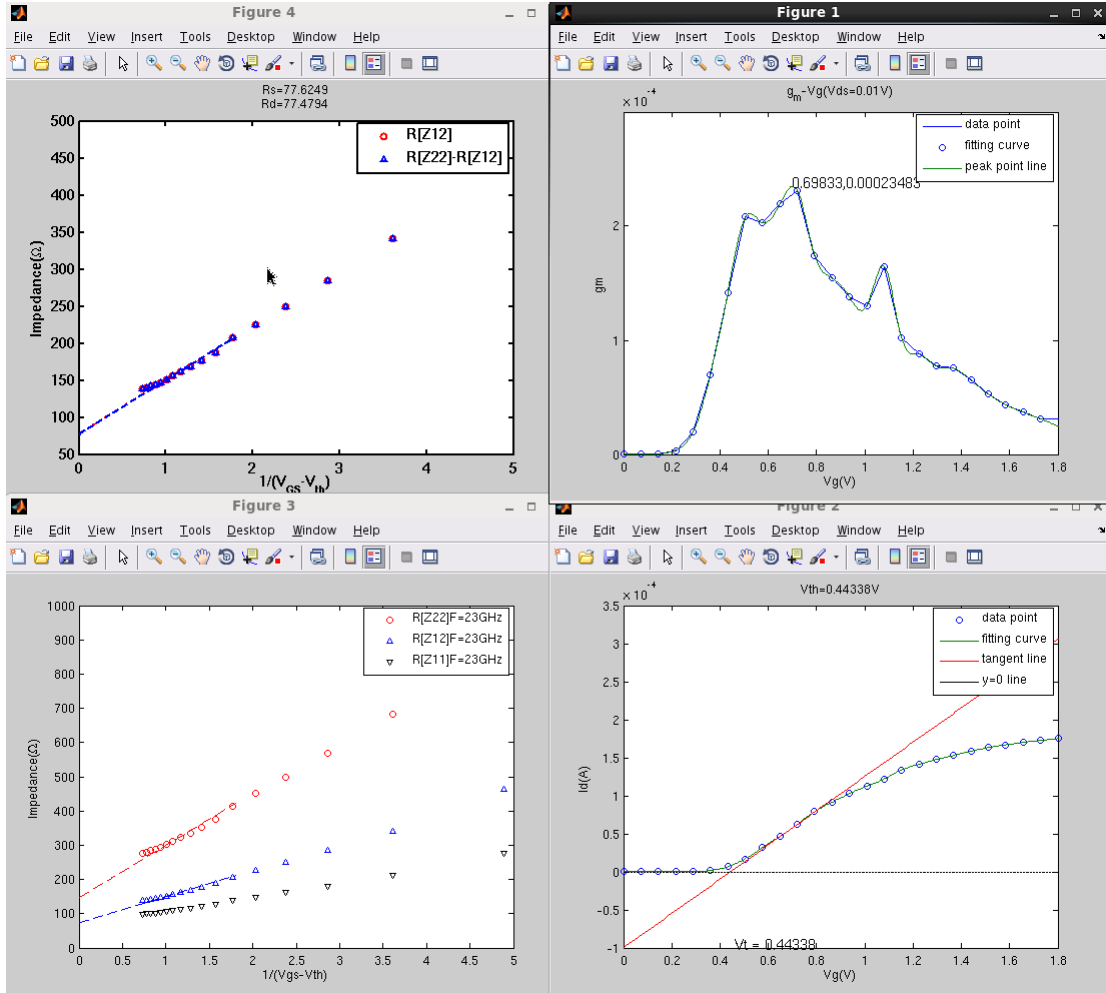


Figure 2.7: Source and drain resistance extraction.

## 2.5 DC I-V Calibration

Drain Induced Barrier Lowering(DIBL), Subthreshold Swing(SS), body effect are important dc characteristics and all need to be calibrated. Details of the calibration for DIBL, SS and body effect are described.

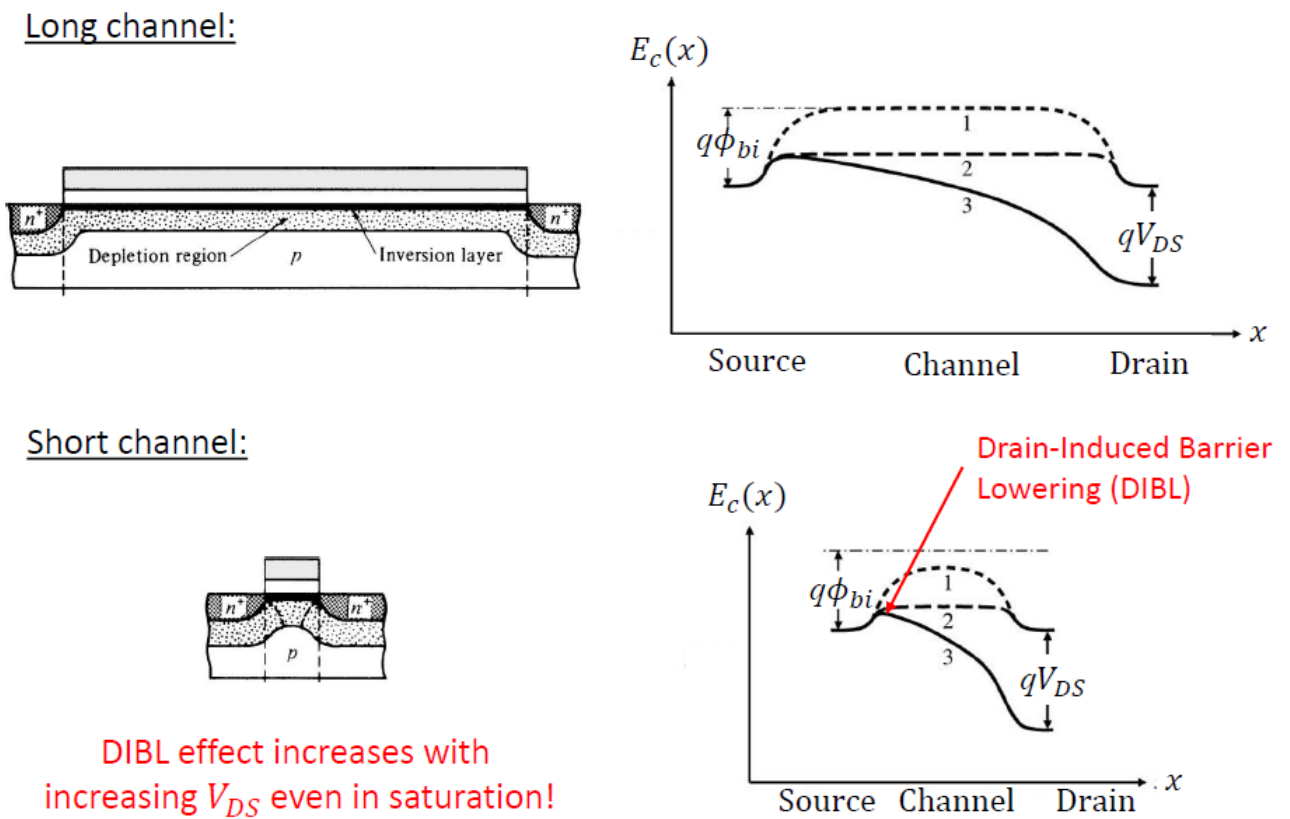
### 2.5.1 DIBL and SS calibration

DIBL is measured by the threshold voltage decrease per volt increase of  $V_{DS}$ . This effect can be clearly seen from the band diagram. DIBL is often described as a change in

the effective threshold. The DIBL calculation is shown:

$$DIBL = \frac{V_{T,lin} - V_{T,sat}}{V_{DD} - V_{DS,sat}}, \quad (2.5)$$

where  $V_{T,lin}$  is the threshold voltage under  $V_{DS} = 0.05V$ , and  $V_{T,sat}$  is the threshold voltage under  $V_{DS} = 1.1V$ . Figure 2.9 shows the band diagram comparison between long-channel device and short-channel device.



Based on Tsividis/McAndrew; Copyright © Oxford University Press, 2011

2

Figure 2.8: Band diagram of long channel and short channel MOSFET devices showing Drain Induced Barrier Lowering effect[15].

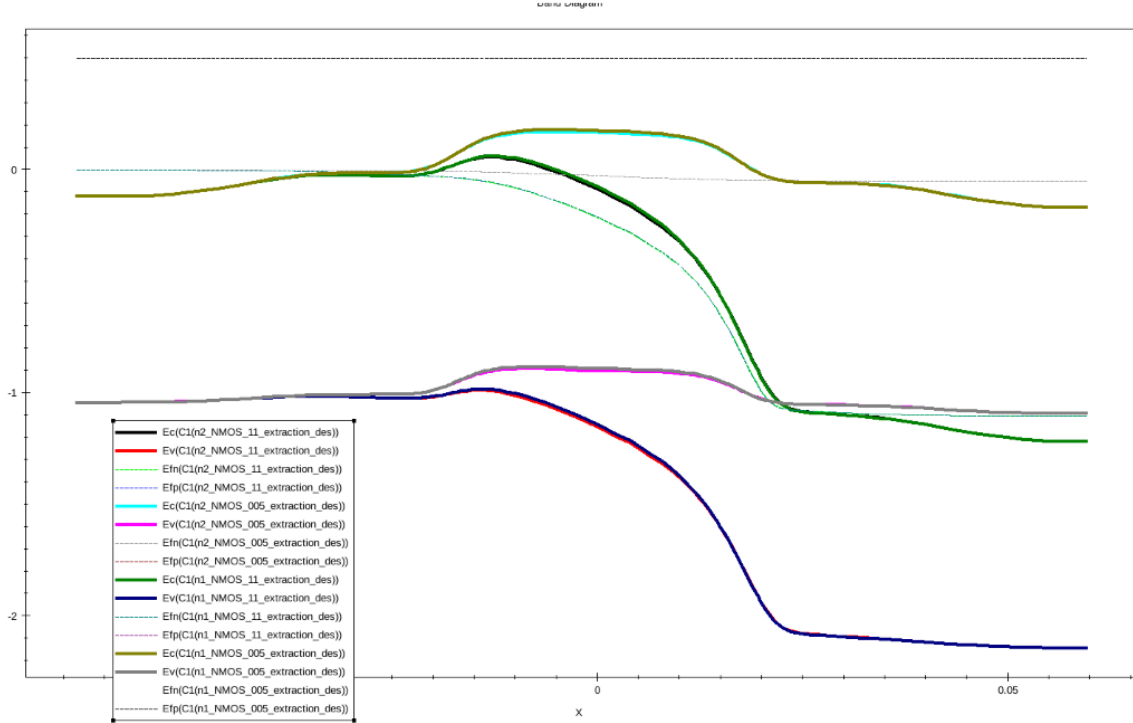


Figure 2.9: Simulated band diagram of 28nm gate length device for Drain Induced Barrier Lowering effect illustration.

Subthreshold swing(SS) is another important MOSFET dc characterization. Subthreshold swing can be defined as the voltage change per decade decrease in drain current. This characteristics along with DIBL can be seen and calculated from  $I_{DS} - V_{GS}$  curves. Figure 2.10 illustrates the definition of DIBL and SS. SS can be calculated using:

$$SS = V_{gs_{I_{ds}=1000nA}} - V_{gs_{I_{ds}=100nA}}, \quad (2.6)$$

where  $V_{gs_{I_{ds}=1000nA}}$  is the gate to source voltage when drain current is equal to  $1000nA$  and  $V_{gs_{I_{ds}=100nA}}$  is the gate to source voltage when drain current is equal to  $100nA$ .

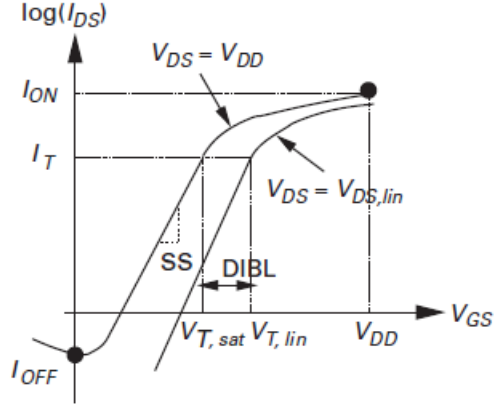


Figure 2.10: DIBL and SS calculation illustration.

$I_{DS} - V_{GS}$  are simulated when  $V_{DS} = 0.05V$  for linear condition, and at  $V_{DS} = 1.1V$  for saturation condition. DIBL and SS are very sensitive to halo doping profile and channel doping profile. By calibrating the peak value of halo doping and channel doping, the simulation  $I_{DS} - V_{GS}$  curve can fit the measurement data.

Figure 2.11 shows I-V curves before calibration, simulation biases are:  $V_{DS} = 0.05V$ ,  $V_{DS} = 0.4V$ ,  $V_{DS} = 0.75V$ ,  $V_{DS} = 1.0V$  for each four. Figure 2.12 shows the simulation result after setting peak halo doping to  $5.5 \times 10^{18}/cm^3$  and channel peak doping to  $1 \times 10^{18}/cm^3$  under the same bias conditions. Figure 2.13 gives the final calibration result for DIBL and SS.

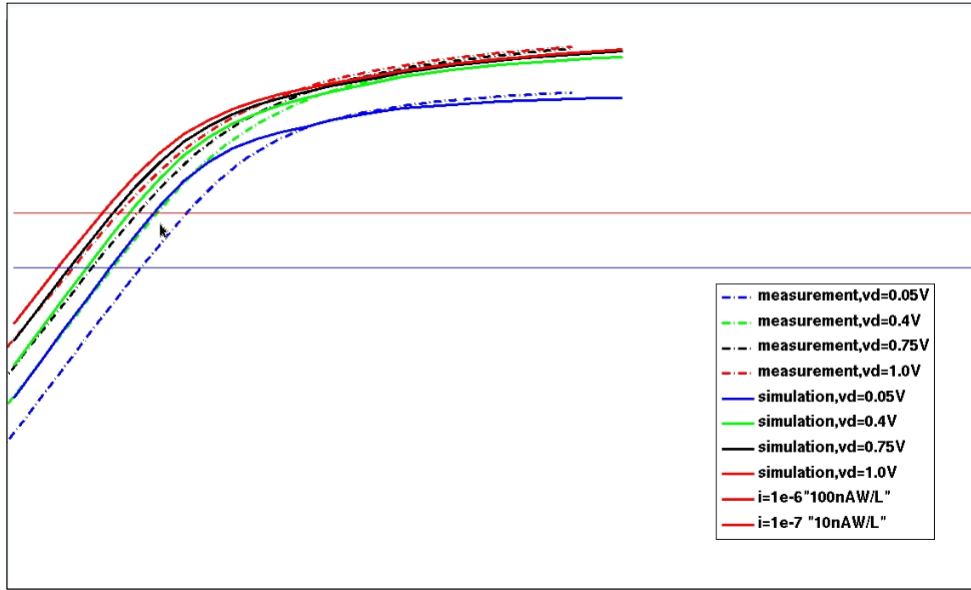


Figure 2.11: Simulated  $I_{DS} - V_{DS}$  curves before DIBL and SS calibration.

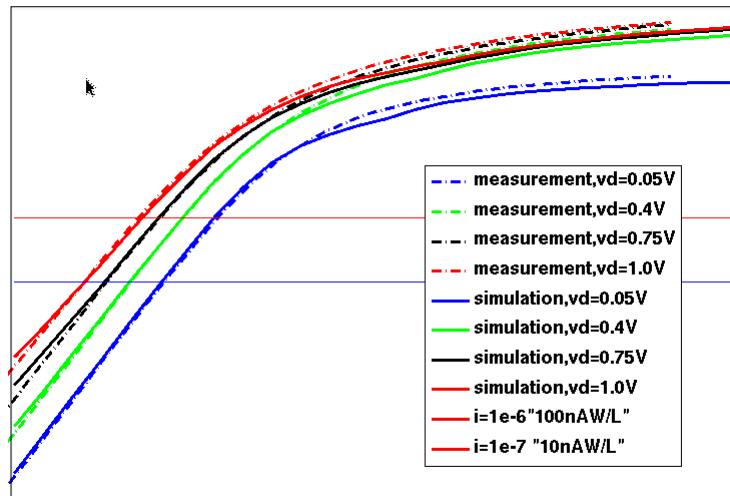


Figure 2.12: Simulated  $I_{DS} - V_{DS}$  curves when  $V_{DS} = 0.05V$ ,  $V_{DS} = 0.4V$ ,  $V_{DS} = 0.75V$ ,  $V_{DS} = 1.0V$ .

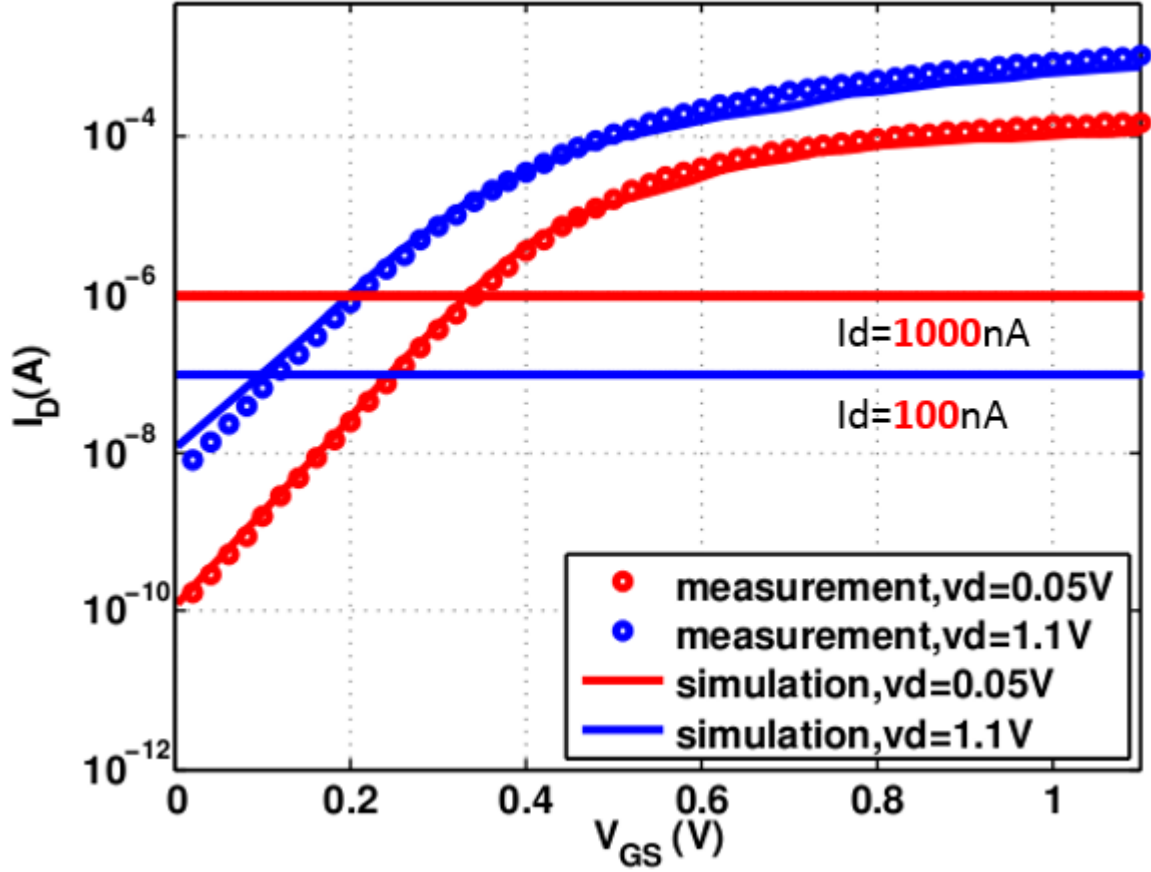


Figure 2.13: DIBL and SS Calibration illustration.

Two lines  $I_{ds} = 1000nA$  and  $I_{ds} = 100nA$  are introduced for DIBL and SS calculation. By applying both measurement and simulation data to this equation, I calculated and compared the two DIBL values. The measurement data are  $DIBL_{mea} = \frac{V_{T,lin} - V_{T,sat}}{V_{DD} - V_{DS,sat}} = 0.1368$  and  $SS_{mea} = V_{gs_{I_{ds}=1000nA}} - V_{gs_{I_{ds}=100nA}} = 0.0975$ . For simulation data,  $DIBL_{sim} = \frac{V_{T,lin} - V_{T,sat}}{V_{DD} - V_{DS,sat}} = 0.1373$  and  $SS_{mea} = V_{gs_{I_{ds}=1000nA}} - V_{gs_{I_{ds}=100nA}} = 0.0997$ .

### 2.5.2 Body Effect calibration

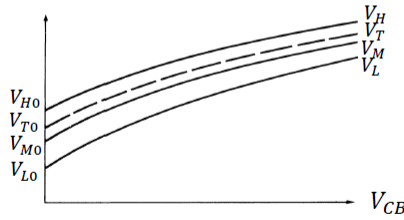
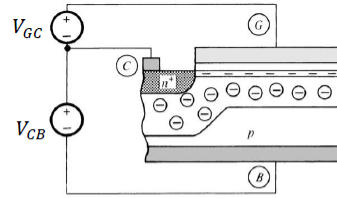
DIBL and SS calibration are made under zero body bias condition, body effect calibration is also needed. Body effect is generally discussed in 3-terminal MOS structure. When

$V_{cb}$  is increasing, the level of inversion decreases unless also increase  $V_{GC}$  by an appropriate amount[1].

### Body effect

$$V_{CB} \nearrow \Rightarrow |Q'_i| \searrow \text{ for fixed } V_{GC}$$

To keep  $Q'_i$  at the same level, we must increase  $V_{GC}$



$V_L, V_M, V_H$  represent the onset of weak, moderate, and strong inversion

"Body effect coefficient"

E.g., 
$$V_M = V_{FB} + 2\phi_F + \gamma\sqrt{\phi_F + V_{CB}}$$

$$\gamma = \frac{\sqrt{2q\epsilon_s N_A}}{C'_{ox}}$$

Figure 2.14: Body Effect Introduction[16].

This effect is mainly affected by substrate doping. Meanwhile, other parameter values such as halo junction depth, LDD depth and channel doping can also affect body effect. This effect can also be seen from the  $V_{TH}$  change in  $I_{DS} - V_{GS}$  curves under multiple  $V_{DS}$ . This section will give an summary of body effect dependence. In simulation steps, multiple body bias values are applied for the same  $V_{DS}$  and  $V_{GS}$ . The depletion layer will change with different body biases. Simulations are done under zero body bias and  $-0.25V$  body bias. The changes with different body biases can be observed:

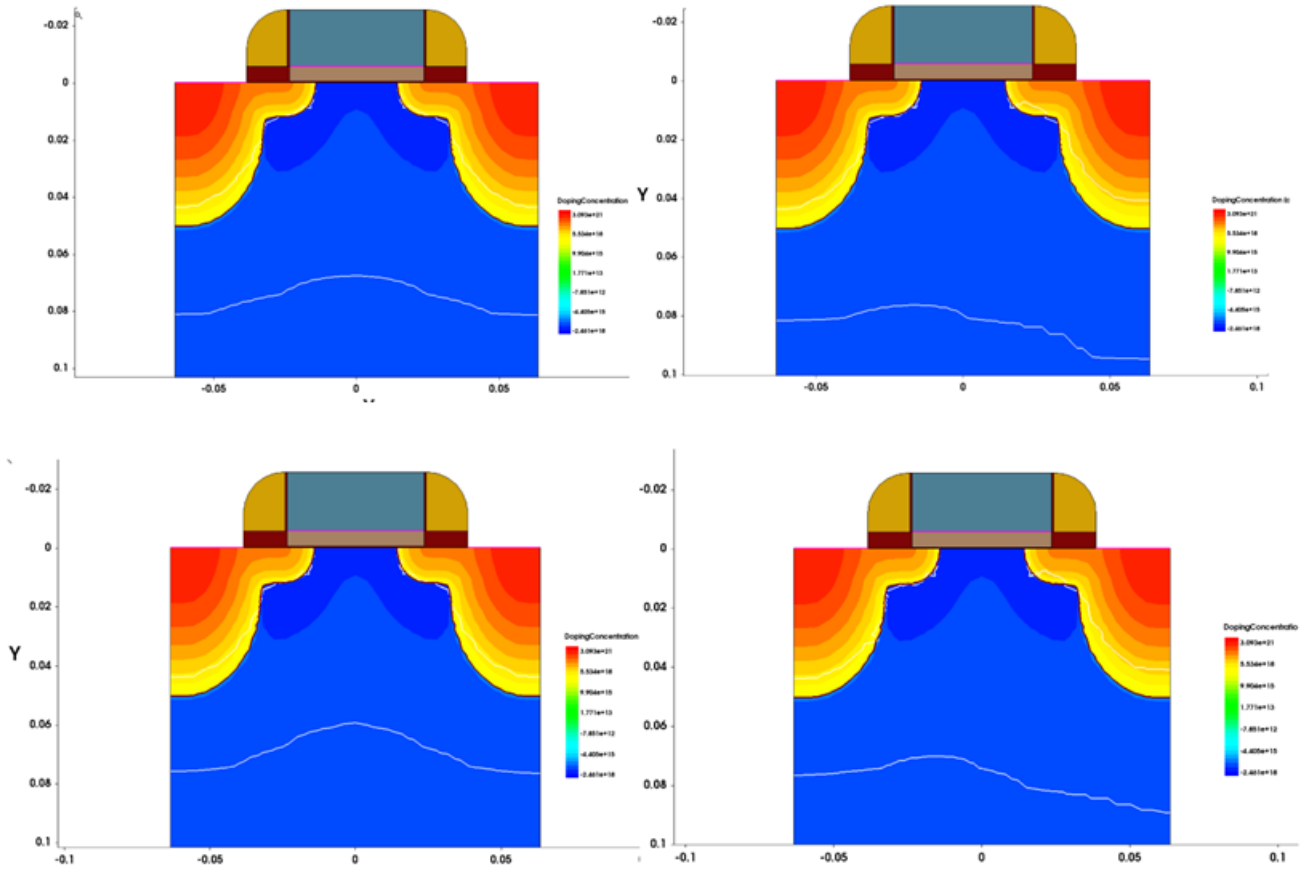


Figure 2.15: Depletion layer change under different body bias.

### Substrate doping calibration

Constant doping profile is used for substrate doping in simulation devices. Three different substrate doping values are applied in this experiment. By running  $I_{ds} - V_{gs}$  curve simulation and comparing the simulated and measured data curves. The substrate bias is also given 3 values:  $V_{gb} = 0V, V_{gb} = -0.25V, V_{gb} = -0.5V$ . If the simulated  $I_{ds} - V_{gs}$  curve can fit the measurement data under all three substrate bias values, the appropriate substrate doping can be determined.

# Substrate doping

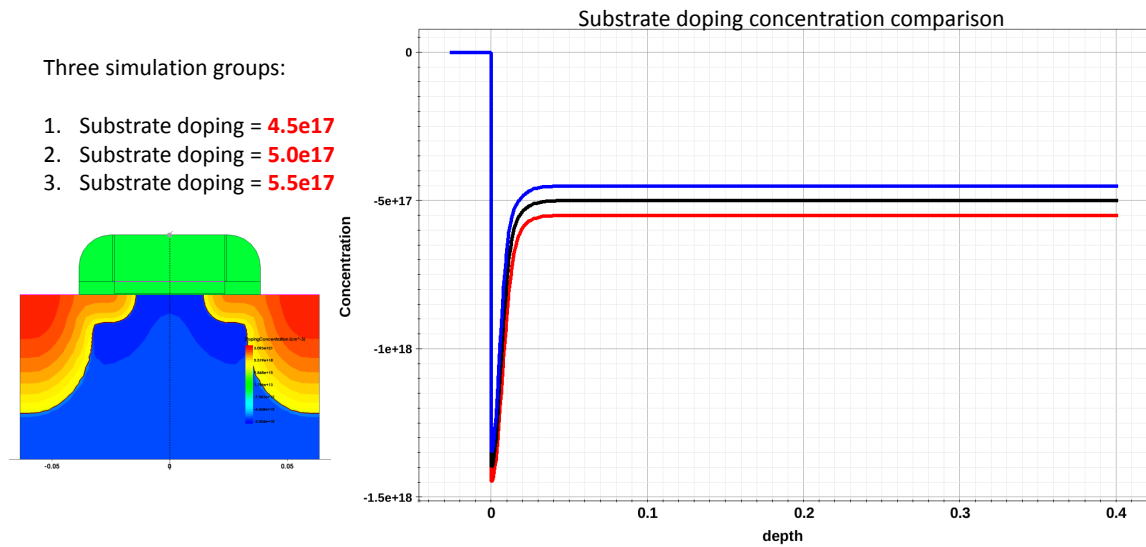


Figure 2.16: Substrate doping simulation illustration.

Figure 2.16 shows how the substrate doping profile when doing a vertical cut along the middle of device. With 3 different doping values, the doping difference mostly took place at the substrate region. Figure 2.17 shows the results of simulation.

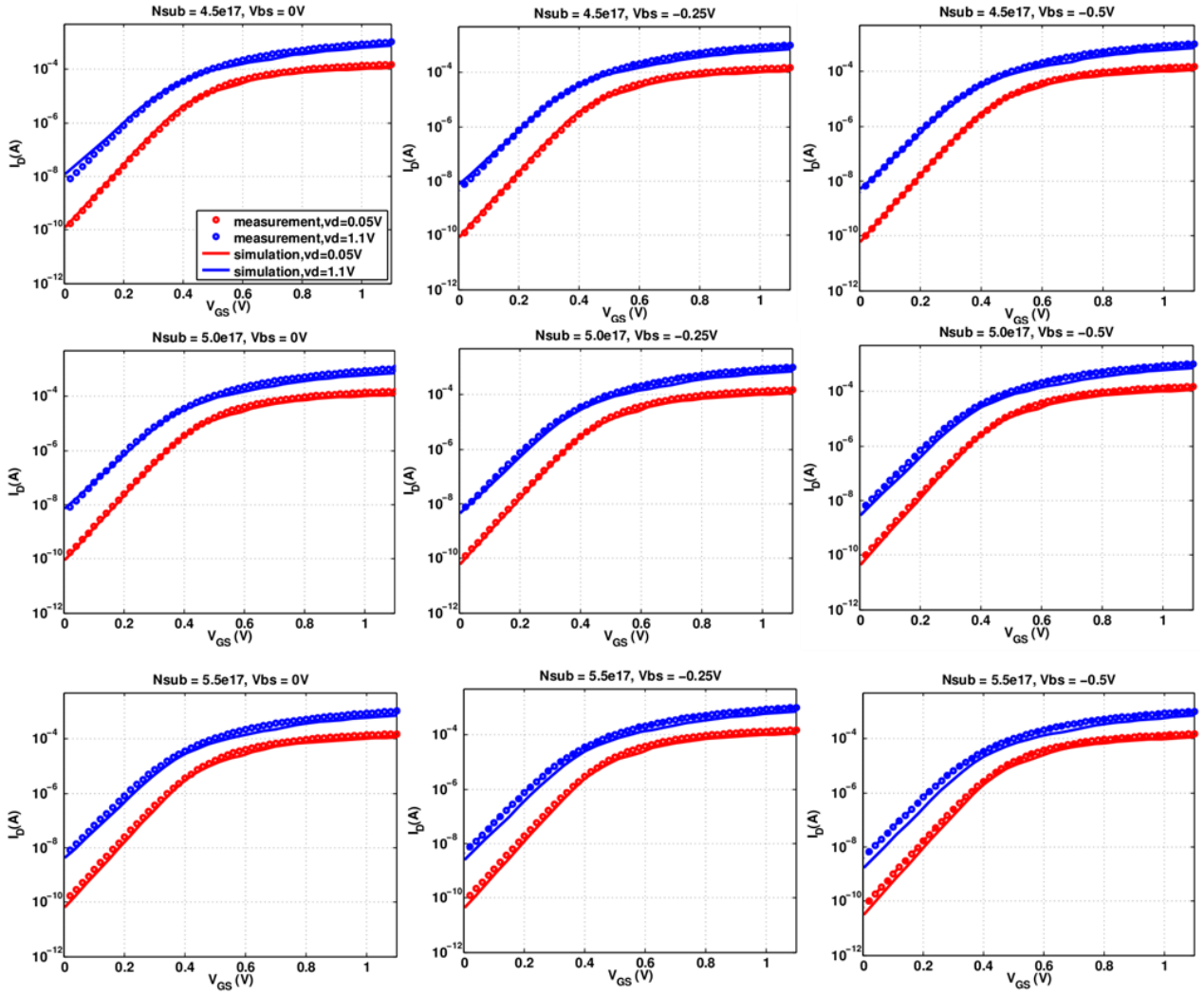


Figure 2.17: Substrate doping impact on body effect.

The second group of simulation results fit the measurement data best for all three body biases. Thus the substrate doping is determined. For the first group, curves can not fit under body bias equal to zero, and as the third group, curves are not match when body bias equals  $-0.25V$  and  $-0.5V$ .

## Halo doping calibration

Halo doping can also affect body effect, so it is necessary to calibrate halo doping profiles. In the simulation device, halo doping is placed as a Gaussian profile and Gaussian profile is determined mainly by two parameters, peak concentration and junction depth. These two parameters will be discussed separately in this section. In halo doping peak concentration calibration and halo doping depth calibration, also three different parameter values are set for corresponding simulation steps.

## Halo doping concentration

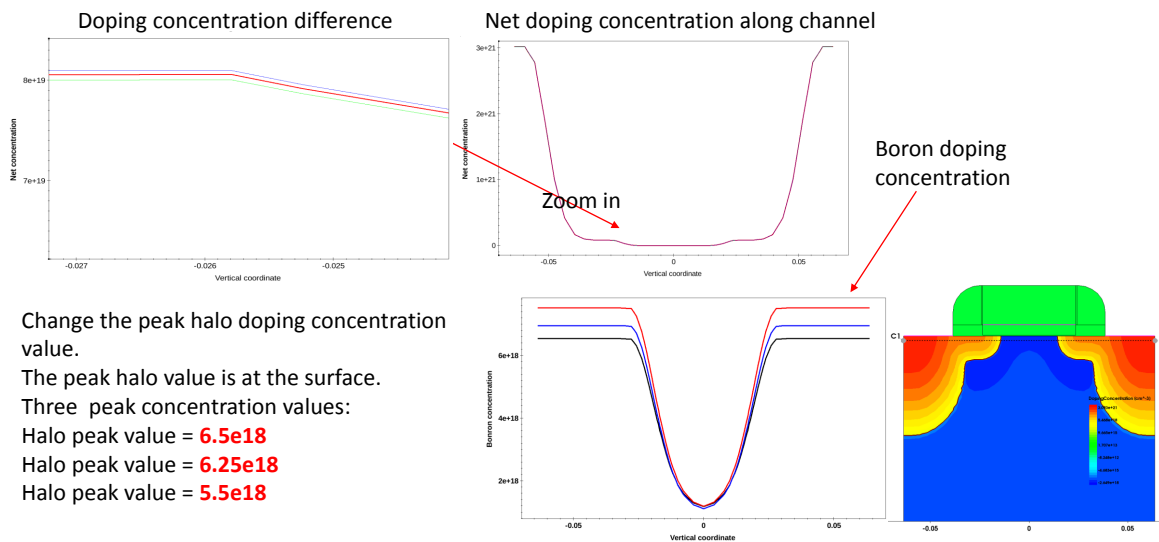


Figure 2.18: Halo doping peak concentration simulation.

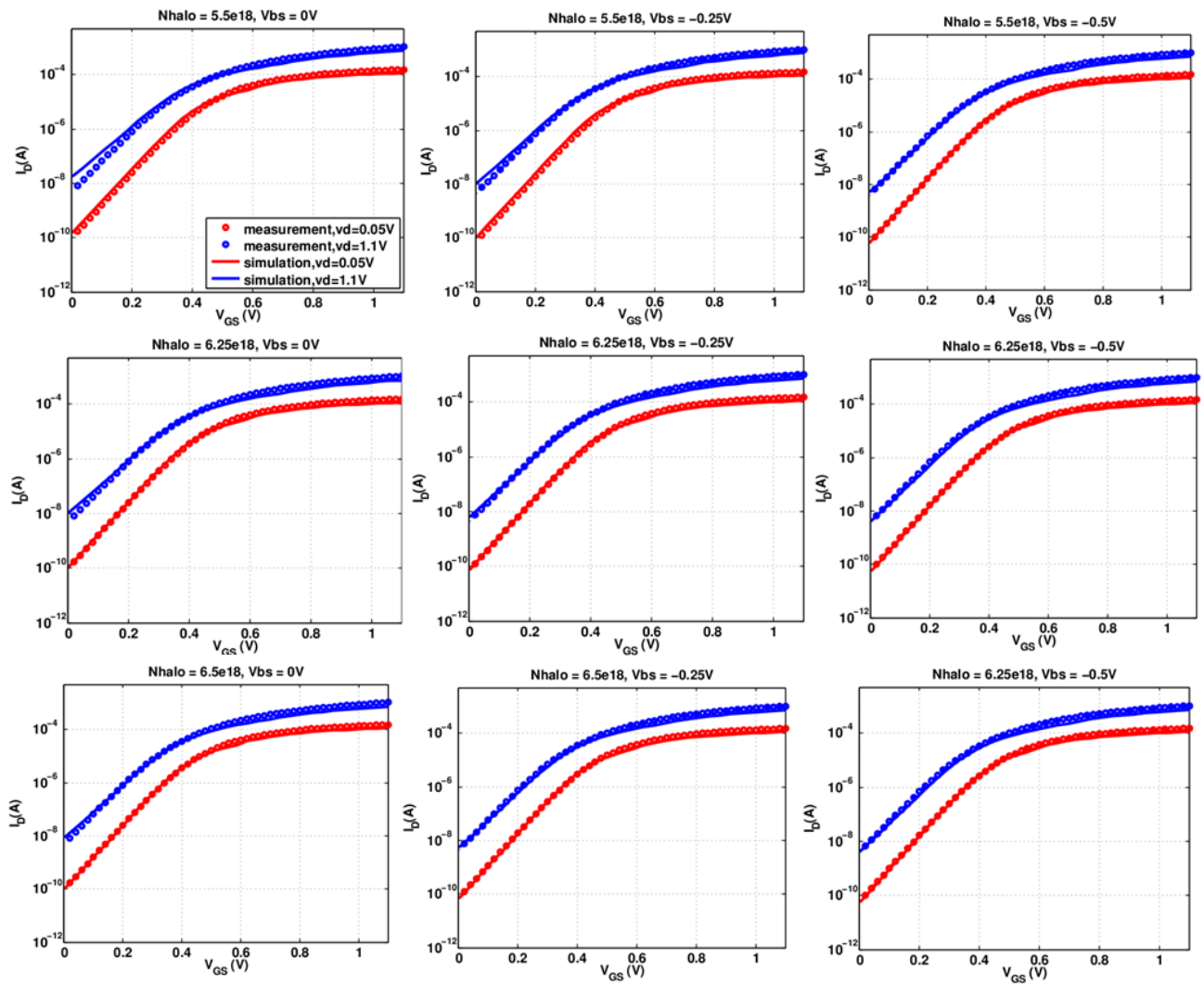


Figure 2.19: Halo peak concentration impact on body effect.

# Halo junction depth

Since halo doping is an Gaussian doping profile. Besides doping peak value, junction depth is also an important parameter to consider

Xjhalo = **0.025um**(originally)  
 Xjhalo = **0.022um**  
 Xjhalo = **0.028um**

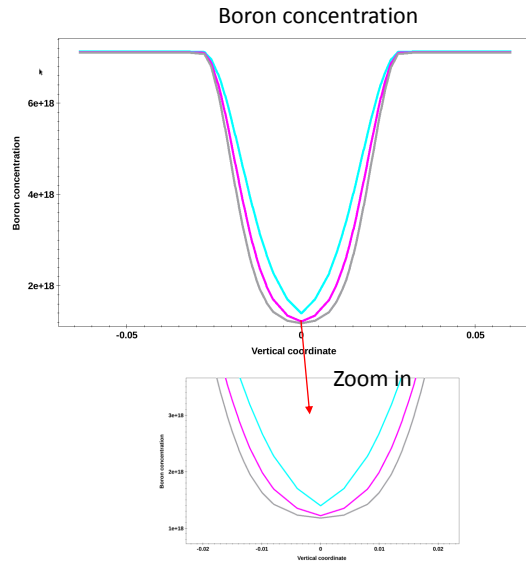
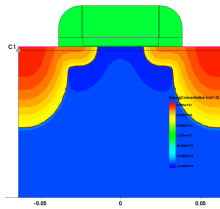


Figure 2.20: Halo doping depth simulation.

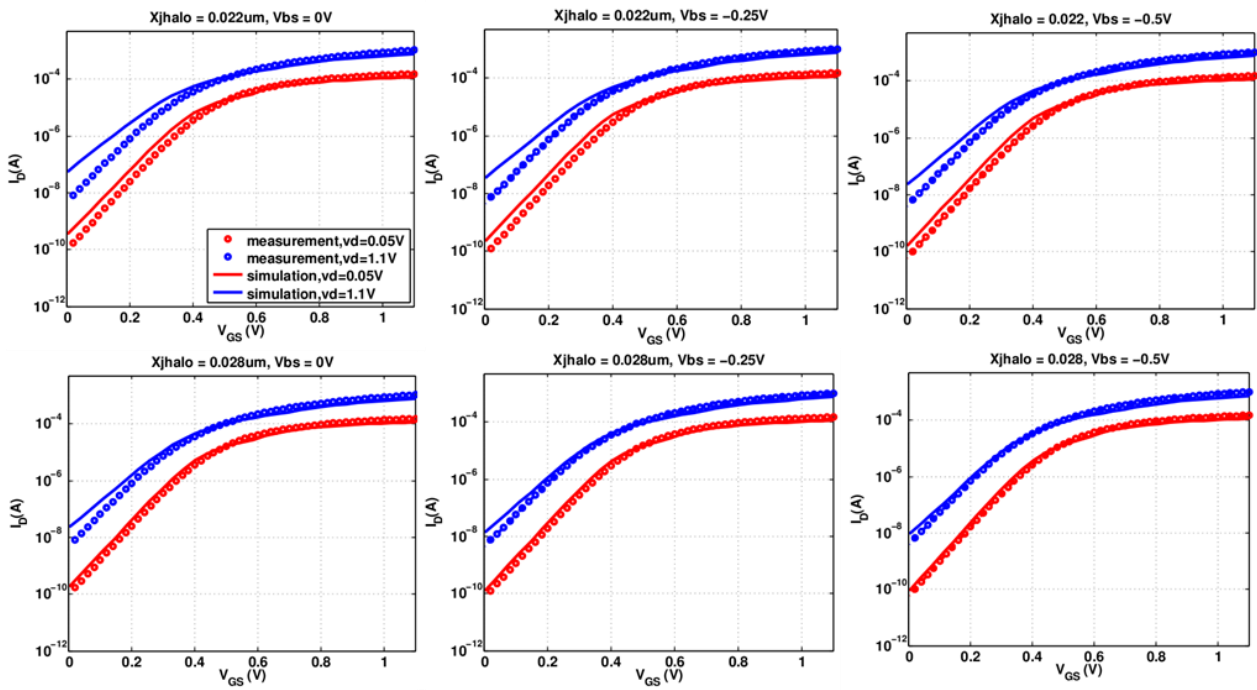


Figure 2.21: Halo depth impact on body effect.

From the simulation results, the peak halo doping concentration and junction depth can be calibrated in which process, can determine the whole halo doping profile. Besides, from these simulation results, it can be concluded that changing halo doping depth parameter in the simulation will significantly change the DIBL and SS value, and its value can not be changed after the DIBL and SS calibration.

### Channel doping concentration calibration

In the DIBL and SS calibration step, Gaussian doping profile is added into the channel region in order to fit the measured DIBL and SS at the same time. This Gaussian doping profile is named as channel doping profile. However, this channel region doping, can also affect body effect, so simulations should be taken for impact analysis.

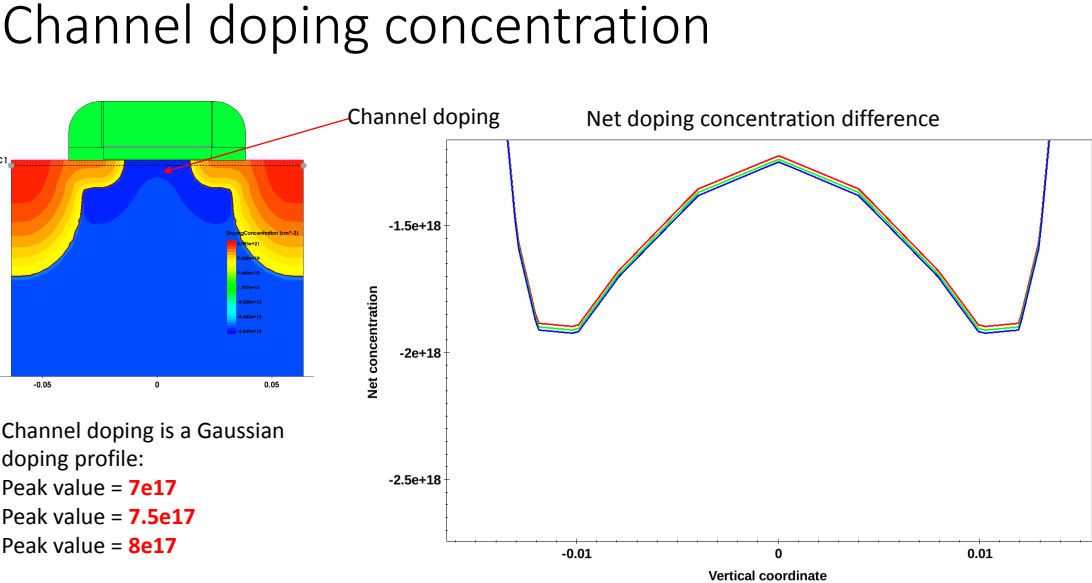


Figure 2.22: Channel doping simulation.

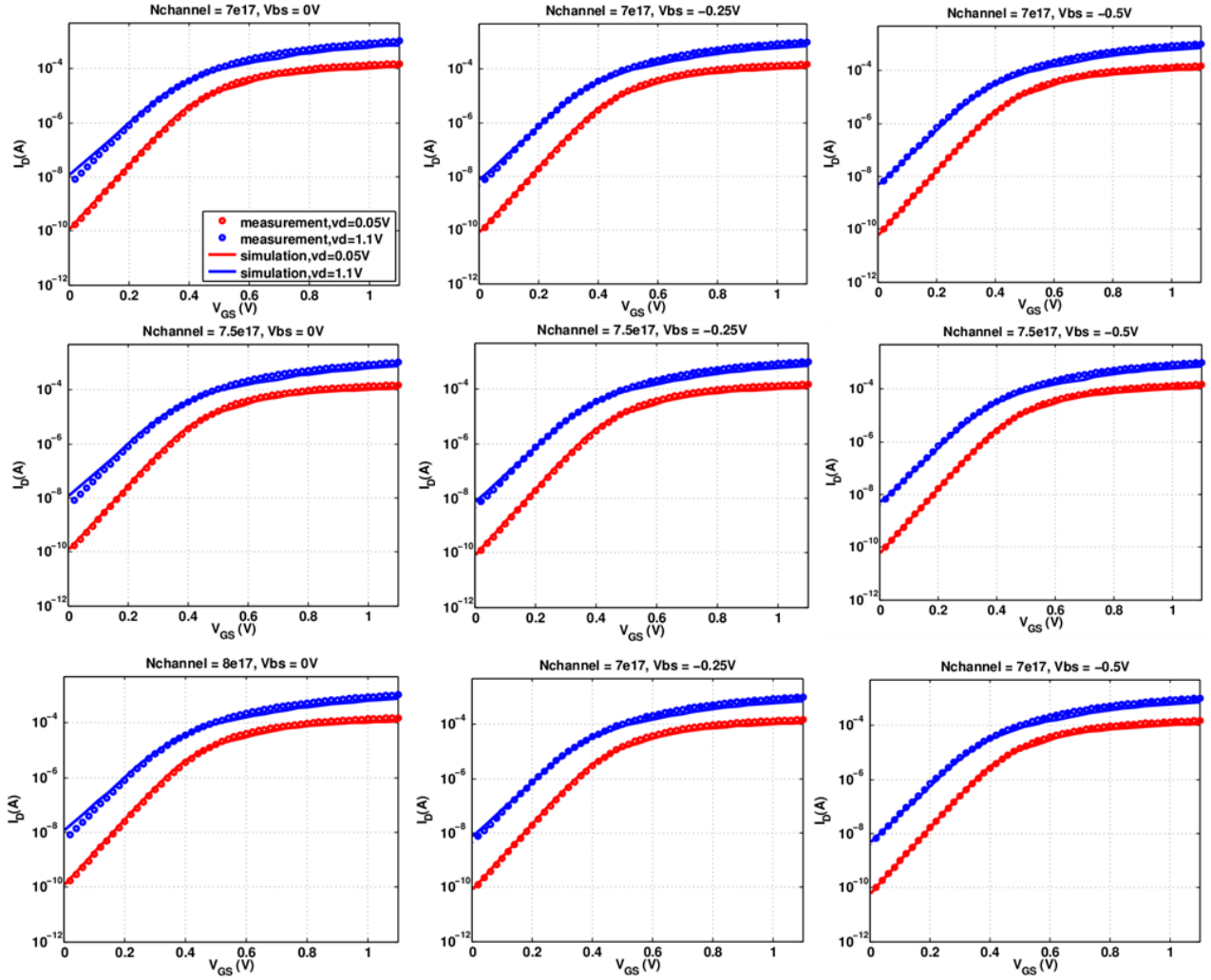


Figure 2.23: Channel doping impact on body effect.

In the simulation results, the  $I_{DS} - V_{GS}$  curves are not changing remarkably. So this channel doping profile is not affecting body effect prominently.

### Source and drain extension doping profile calibration

Source and drain extension refers to LDD n- region in the top of source and drain region. In the previous step, this profile's peak doping concentration is calibrated for a specific  $R_s$  and  $R_d$  value, so there's no need for peak doping concentration discussion. This section will have an analysis on how this profile influence body effect.

## Source & Drain extension junction depth

- $X_{j\_ext} = 0.012\mu\text{m}$  (Calibrated after DIBL and SS calibration)
- $X_{j\_ext} = 0.01\mu\text{m}$

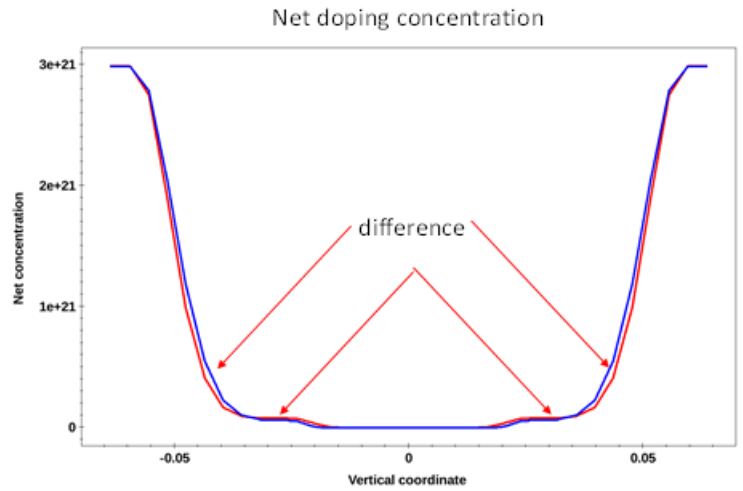
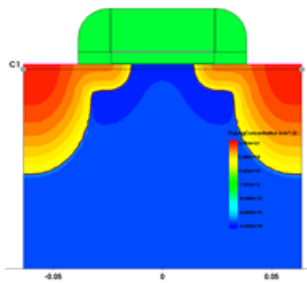


Figure 2.24: Source and drain extension doping simulation.

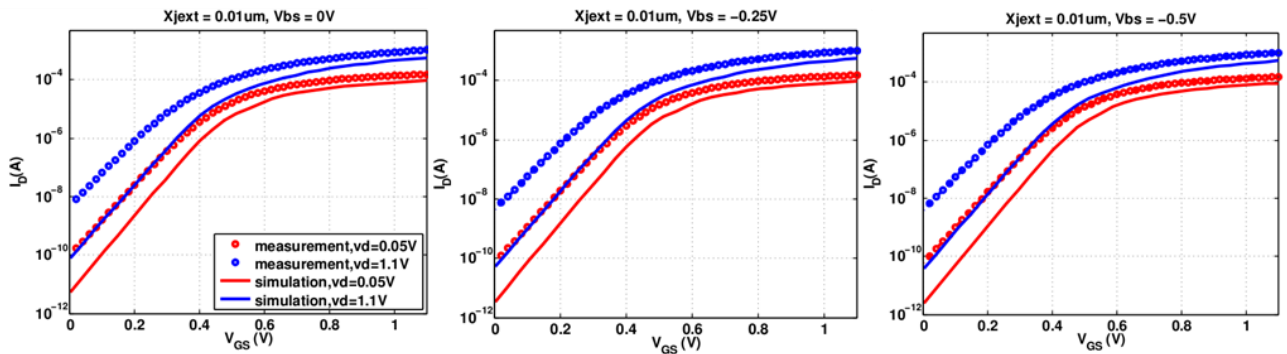


Figure 2.25: Source and drain extension doping impact on body effect.

## Source and drain doping profile calibration

Source and drain region is another factor needs consideration for body effect. Since in  $R_s$  and  $R_d$  calibration the peak doping concentration of the profile is calibrated, then in this step, junction depth is the only parameter to analysis.

## Source & Drain junction depth

$X_{j\_S/D} = 0.05\mu\text{m}$  (Calibrated after DIBL and SS calibration)

$X_{j\_S/D} = 0.045\mu\text{m}$

$X_{j\_S/D} = 0.055\mu\text{m}$

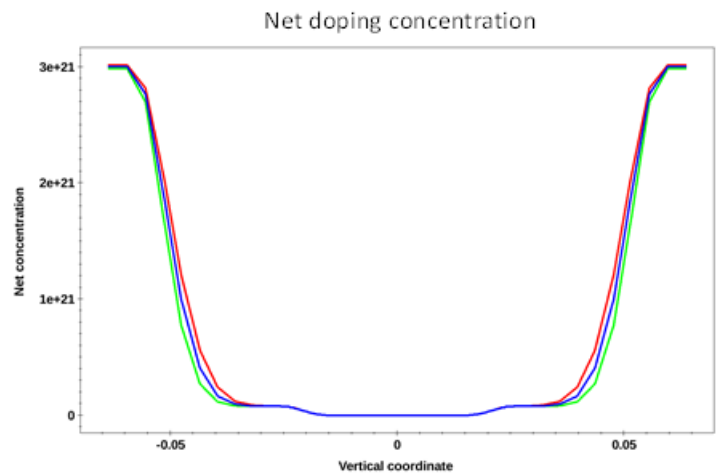
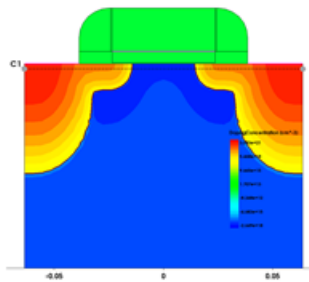


Figure 2.26: Source and drain extension doping simulation.

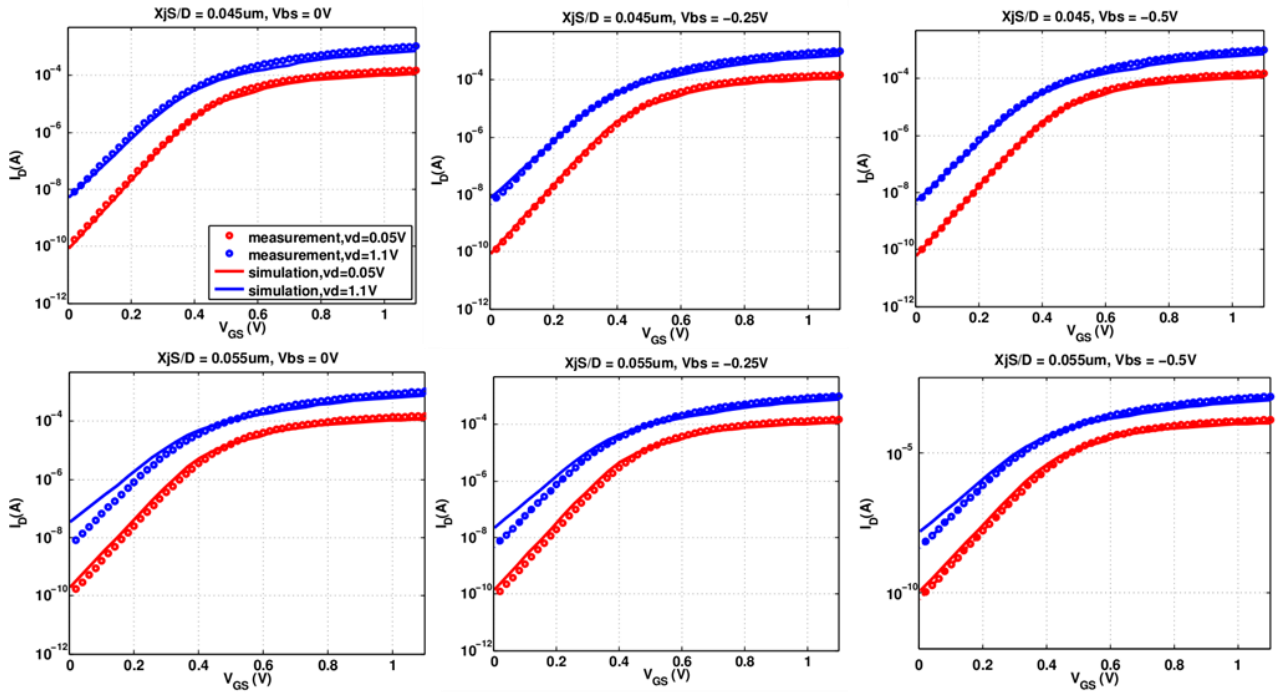


Figure 2.27: Source and drain extension doping impact on body effect.

Then after this simulation step, the final calibrated important doping profiles are determined. Then mobility model parameters need to be calibrated.

## 2.6 Physics Model Calibration

Carrier mobilities calibration are required in order to obtain reasonable  $I - V$  characteristic. In TCAD Sentaurus Device simulation, a modular approach is used for carrier mobilities. There are several carrier mobility descriptions including mobility due to phonon scattering, doping-dependent mobility degradation, carrier-carrier scattering, mobility degradation at interfaces, high field saturation, and energy-dependent mobility. Different mobility descriptions are used under different circumstances, for instance the mobility due to phonon scattering should only be used only for undoped materials, while for doped materials, doping dependent mobility degradation is used. For each carrier mobility description, one or several mobility models are presented.

### 2.6.1 Lombardi Mobility Model

Lombardi mobility model is an empirical model that combines mobility expressions for semiconductor-insulator interfaces and for bulk silicon. Its basic equation is given by Matthiessen's rule[17]:

$$\frac{1}{\mu} = \frac{1}{\mu_b} + \frac{1}{\mu_{ac}} + \frac{1}{\mu_{sr}}, \quad (2.7)$$

where  $1/\mu_{ac}$  and  $1/\mu_{sr}$  are surface contribution due to acoustic phonon scattering and contribution attributed surface roughness scattering. These two mobility parameters can be defined using:

$$\mu_{ac} = \frac{B}{F_{\perp}} + \frac{C((N_{A,0} + N_{D,0} + N_2)/N_0)^{\lambda}}{F_{\perp}^{1/3}(T/300K)^k}, \quad (2.8)$$

$$\mu_{sr} = \left( \frac{(F_{\perp}/F_{ref})^{A^*}}{\delta} + \frac{F_{\perp}^3}{\eta} \right)^{-1}, \quad (2.9)$$

where the reference field  $F_{ref} = 1V/cm$ ,  $F_{\perp}$  is the transverse electric field normal to the semiconductor insulator interface. In Lombardi model, the exponent  $A^*$  is equal to 2. Then by setting  $\mu_s = \frac{1}{\mu}$ ,  $\mu_s$  is the total electron or hole mobility accounting for surface effect combining the two contributions.  $\mu_b$  is mobility in silicon bulk.  $\mu_b$  includes mobility due to phonon scattering  $\mu_{const}$  and doping dependent mobility  $\mu_{dop}$ ,  $\mu_{const}$  can be calculated by:

$$\mu_{const} = \mu_L \left( \frac{T}{300K} \right)^{\xi}, \quad (2.10)$$

where  $\mu_L$  is the mobility due to bulk phonon scattering. The default values of  $\mu_L$  and the experiment  $\xi$  are listed in the table below:

| Symbol  | Parameter name | Electrons | Holes | Unit      |
|---------|----------------|-----------|-------|-----------|
| $\mu_L$ | mumax          | 1417      | 470.5 | $cm^2/Vs$ |
| $\xi$   | exponent       | 2.5       | 2.2   | 1         |

Table 2.1: Constant mobility default coefficient.

The equations for doping dependent model is given by:

$$\mu_{dop} = \mu_{min1} \exp\left(-\frac{P_C}{N_{tot}}\right) + \frac{\mu_{const} - \mu_{min2}}{1 + (N_{tot}/C_r)^\alpha} - \frac{\mu_1}{1 + (C_s/N_{tot})^\beta}, \quad (2.11)$$

where  $\mu_{min1}$ ,  $\mu_{min2}$  and  $\mu_1$  are reference mobilities, and the reference doping are  $P_C$ ,  $C_r$  and  $C_s$  are reference doping concentrations. The components  $\alpha$ ,  $\beta$  are accessible in the parameter sets. The corresponding values for silicon are given in Table 3.2 while  $\mu_{ac}$  equation is given:

$$\mu_{ac} = \frac{B}{F_\perp} + \frac{C(N_{tot}/N_D)^\lambda}{F_\perp^{1/3}(T/300K)^k} \quad (2.12)$$

| Symbol       | Parameter name | Electrons      | Holes          | Unit      |
|--------------|----------------|----------------|----------------|-----------|
| $\mu_{min1}$ | mumin1         | 52.2           | 44.9           | $cm^2/Vs$ |
| $\mu_{min2}$ | mumin2         | 52.2           | 0              | $cm^2/Vs$ |
| $\mu_1$      | mu1            | 43.4           | 29.0           | $cm^2/Vs$ |
| $P_C$        | Pc             | 0              | $9.23x10^{16}$ | $cm^{-3}$ |
| $C_r$        | Cr             | $9.68x10^{16}$ | $2.23x10^{17}$ | $cm^{-3}$ |
| $C_s$        | Cs             | $3.34x10^{20}$ | $6.10x10^{20}$ | $cm^{-3}$ |
| $\alpha$     | alpha          | 0.680          | 0.719          | 1         |
| $\beta$      | beta           | 2.0            | 2.0            | 1         |

Table 2.2: Doping dependent mobility default coefficients.

Then equations for  $\mu_{sr}$  and  $A^*$

$$\mu_{sr} = \left(\frac{(F_\perp/F_{ref})^{A^*}}{\delta} + \frac{F_\perp^3}{\eta}\right)^{-1} \quad (2.13)$$

$$A^* = A + \frac{(\alpha_{\perp,n}n + \alpha_{\perp,p}p)N_{ref}^V}{(N_{A,0} + N_{D,0} + N_1)^V} \quad (2.14)$$

The reference field  $F_{ref} = 1V/cm$  ensures a unitless numerator.  $F_{\perp}$  is the transverse electric field normal to the semiconductor insulator interface.  $N_{tot}$  is total doping concentration. All other parameters are accessible in the parameter file.

Default parameter value for Lombardi mobility model is shown:

| Symbol    | Parameter name     | Default               | Unit                      |
|-----------|--------------------|-----------------------|---------------------------|
| B         | B                  | $3.61 \times 10^7$    | $cm/s$                    |
| C         | C                  | $1.7 \times 10^4$     | $cm^{5/3}V^{-2/3}/s^{-1}$ |
| $N_0$     | $N_0$              | 1                     | $cm^{-3}$                 |
| $\lambda$ | lambda             | 0.023                 | 1                         |
| k         | k                  | 1.7                   | 1                         |
| $\delta$  | delta              | $3.58 \times 10^{18}$ | $cm^2/Vs$                 |
| $\eta$    | $1 \times 10^{50}$ | $1 \times 10^{50}$    | $cm/s$                    |

Table 2.3: Lombardi mobility model default coefficient.

### 2.6.2 Low field mobility calibration

Physical mobility model calibration is separated to 2 sections: low field and high field. Saturation velocity and energy relaxation time parameter values influence are negligible in low field conditions thus the low field mobility parameters are calibrated first. In the low field simulation is conduct under voltage bias equals  $0.05V$ , and high field is conduct under bias voltage equals  $1.1V$ . Mobility parameter values in Lombardi model are calibrated in order to fit the  $I_{ds} - V_{gs}$  measurement data curve. In this step, two parameter values are calibrated:  $\lambda_e$  and  $\delta_e$ . The  $\lambda_e$  parameter has influence on  $\mu_{ac}$  value, and  $\delta_e$  has influence on  $\mu_{sr}$  value. So changing these two mobility model parameters, together they will change the mobility.

Table 3.4 shows the default value and calibrated value for  $\lambda_e$  and  $\delta_e$ :

| Symbol      | Parameter name | Default     | calibrated  | Unit      |
|-------------|----------------|-------------|-------------|-----------|
| $\lambda_e$ | lambda-e       | 0.023       | 0.1633      | 1         |
| $\delta_e$  | delta-e        | $3.58^{18}$ | $3.58^{19}$ | $cm^2/Vs$ |

Table 2.4: Low field mobility model parameter calibration.

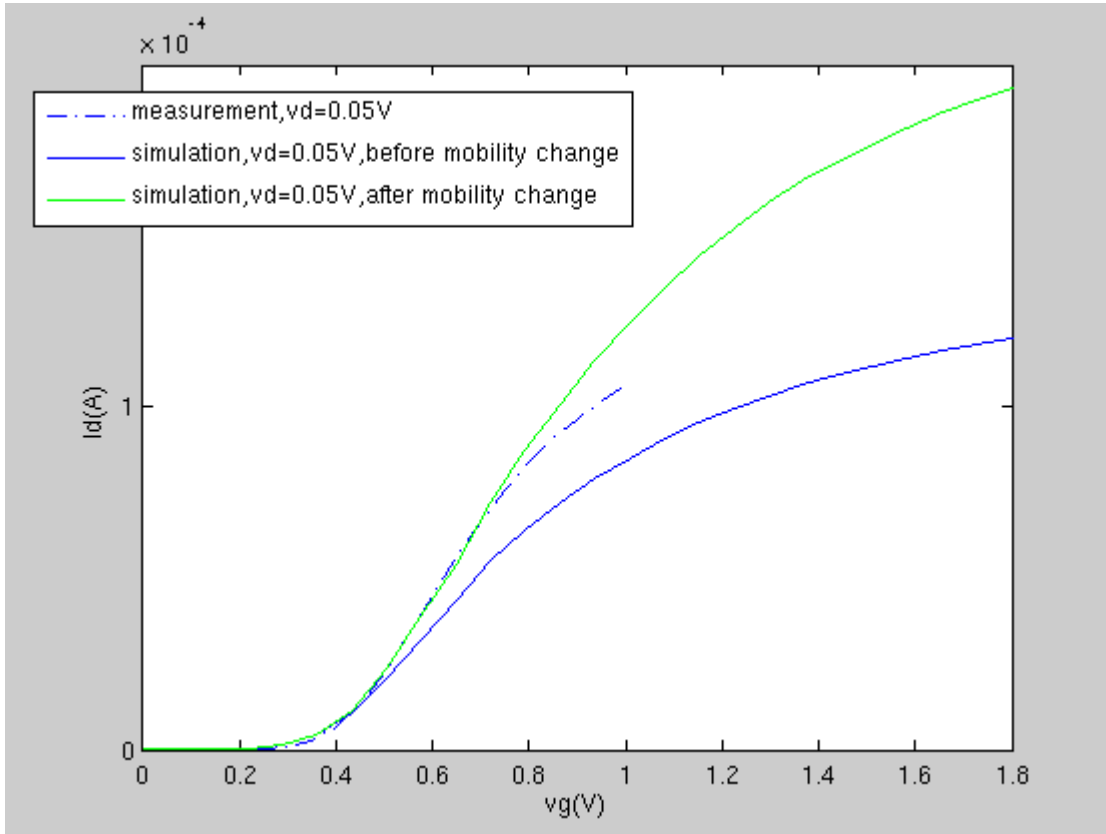


Figure 2.28:  $I_{DS} - V_{GS}$  curve fitting result for low field mobility parameter values under  $V_{ds} = 0.05V$ .

The green line in the Figure 2.28 shows the simulation result after mobility calibration, and this is the figure we can see under low field condition the curves match. Figure 2.29 illustrates the calibrated I-V curve after low field mobility model calibration.

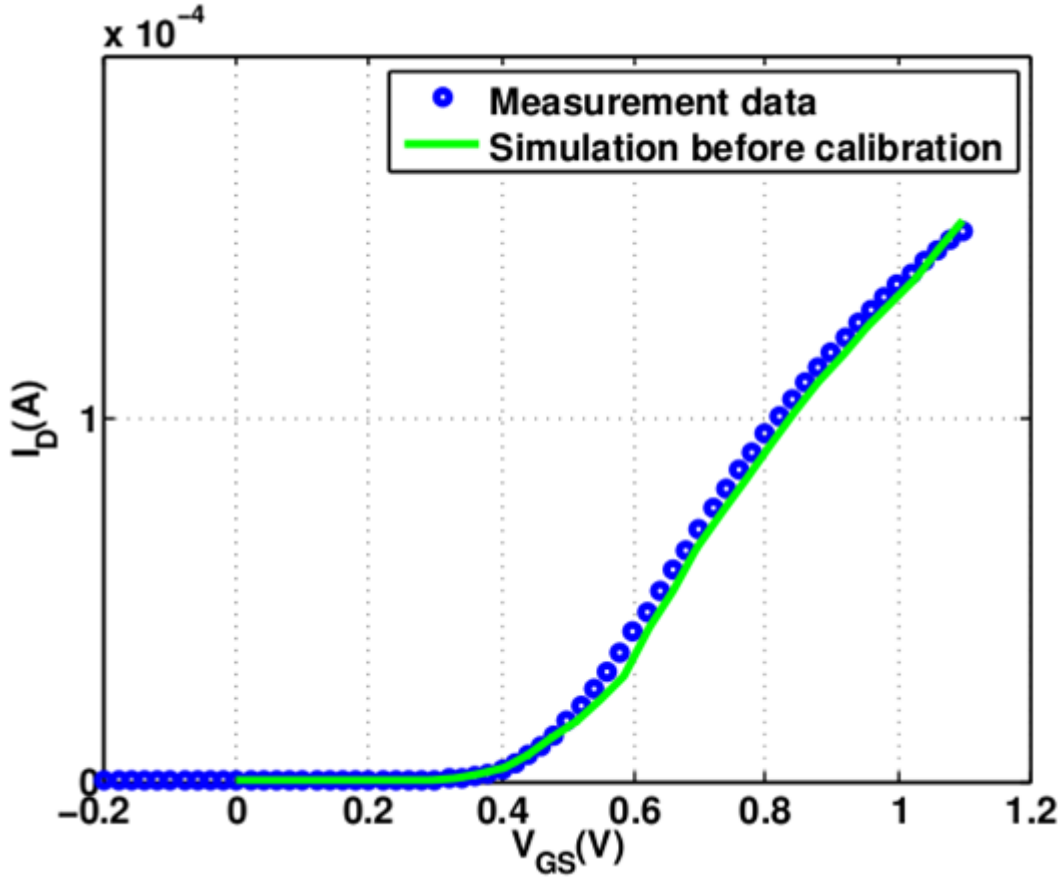


Figure 2.29: Calibrated  $I_{DS} - V_{GS}$  curve illustration for low field mobility parameter values under  $V_{ds} = 0.05V$ .

### 2.6.3 High field mobility calibration

For high field mobility calibration, electron saturation velocity  $V_{sat}$  and electron relaxation time.  $\tau_e$  are adjusted. In TCAD high electric field, the carrier drift velocity is no longer proportional to the electric field, instead, the velocity saturates to a finite speed  $V_{sat}$ . And Sentaurus Device supports two velocity saturation models. Model is part of the Canali model and given by:

$$V_{sat} = V_{sat,0} \left( \frac{300K}{T} \right)^{V_{sat,exp}} \quad (2.15)$$

The default coefficient values are given by:

| Symbol        | Parameter | Electron           | Hole               | Unit        |
|---------------|-----------|--------------------|--------------------|-------------|
| $V_{sat,0}$   | vsat0     | $1.07 \times 10^7$ | $8.37 \times 10^6$ | <i>cm/s</i> |
| $V_{sat,exp}$ | vsatexp   | 0.87               | 0.52               | 1           |

Table 2.5: Velocity saturation parameters.

Two combinations of saturation velocity and energy relaxation time are obtained by fitting the simulation I-V curve to the measurement data. The two combinations are shown in Table 2.6:

| Symbol    | Parameter name | Default           | calibrated 1      | calibrated 2      | Unit        |
|-----------|----------------|-------------------|-------------------|-------------------|-------------|
| $V_{sat}$ | V-sat          | $1.2 \times 10^7$ | $1.2 \times 10^7$ | $1.3 \times 10^7$ | <i>cm/s</i> |
| $\tau_e$  | tau-e          | 0.007             | 0.02              | 0.007             | <i>s</i>    |

Table 2.6: High field mobility parameter calibration.

Then after high field mobility calibration, for both combinations,  $I_{DS} - V_{GS}$  curve can fit the measurement data:

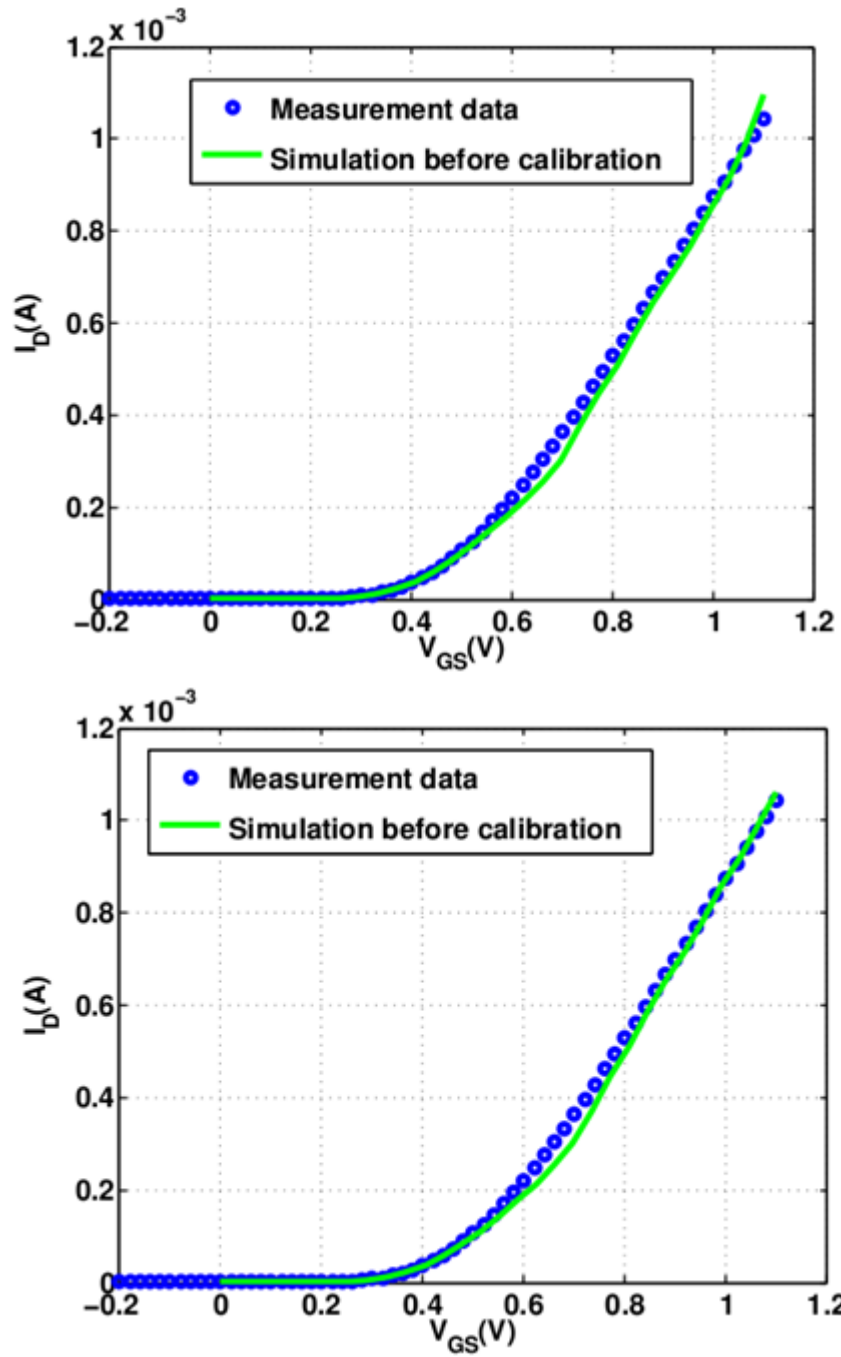


Figure 2.30:  $I_{DS} - V_{GS}$  curve fitting result using calibrated mobility parameter values for both parameter combinations under  $V_{DS} = 1.1V$ .

For multiple  $V_{DS}$  or  $V_{GS}$  biases, with the calibrated mobility parameters, curves are all fit for both  $I_{DS} - V_{gs}$  curves and  $I_{DS} - V_{DS}$  curves. Four different  $V_{DS}$  bias values:  $0.05V$ ,  $0.4V$ ,  $0.6V$ ,  $1.1V$  are set; five bias values for  $V_{DS}$ :  $0.3V$ ,  $0.5V$ ,  $0.7V$ ,  $0.9V$ ,  $1.1V$  and the results are shown in Figure 2.31

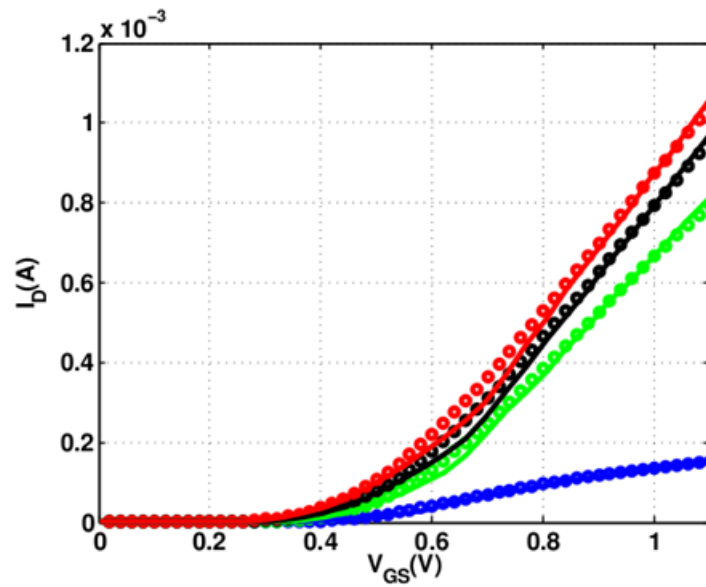


Figure 2.31:  $I_{DS} - V_{GS}$  curve linear scale fitting result with  $V_{GS}$ :  $0.05V$ ,  $0.4V$ ,  $0.6V$ ,  $1.1V$  .

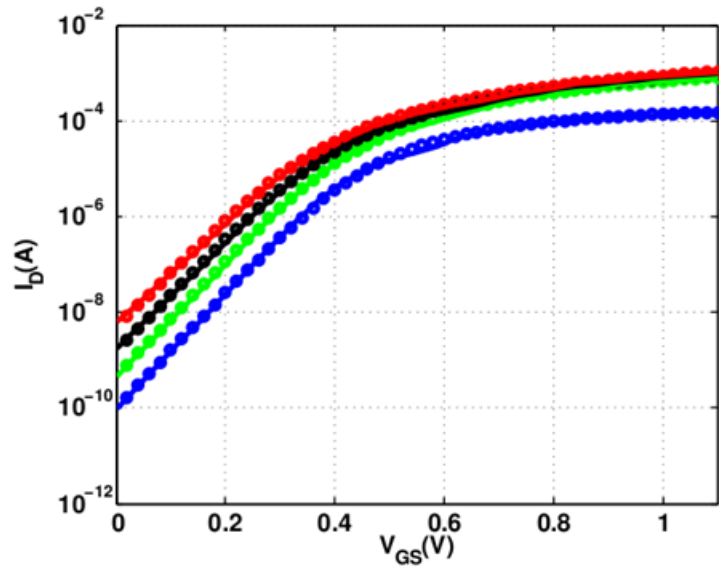


Figure 2.32:  $I_{DS} - V_{GS}$  curve log scale fitting result with  $V_{GS}$ : 0.05V, 0.4V, 0.6V, 1.1V.

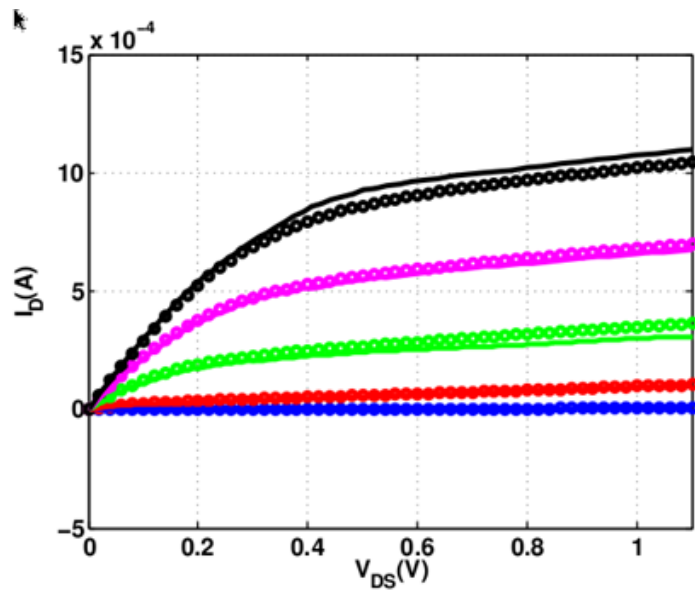


Figure 2.33:  $I_{DS} - V_{DS}$  curve linear scale fitting result with multiple biases using  $\tau = 0.02ps$ ,  $V_{sat} = 1.2e7cm/s$ .

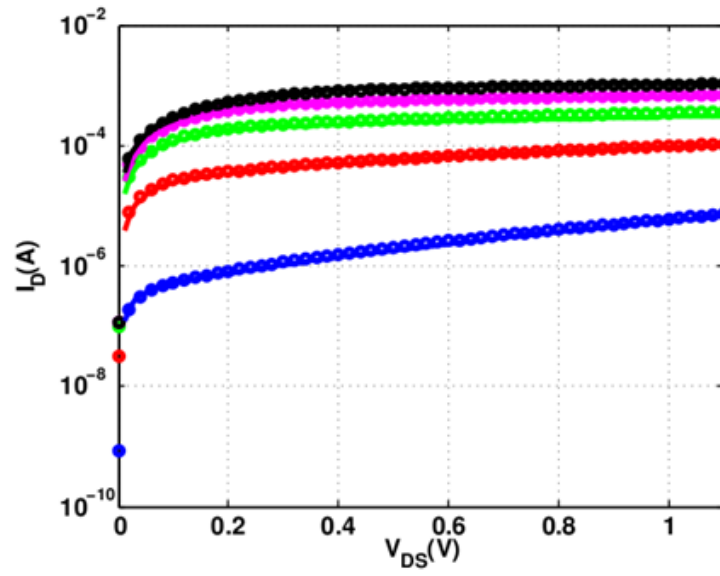


Figure 2.34:  $I_{DS} - V_{DS}$  curve log scale fitting result with multiple biases using  $\tau = 0.02ps$ ,  $V_{sat} = 1.2e7cm/s$ .

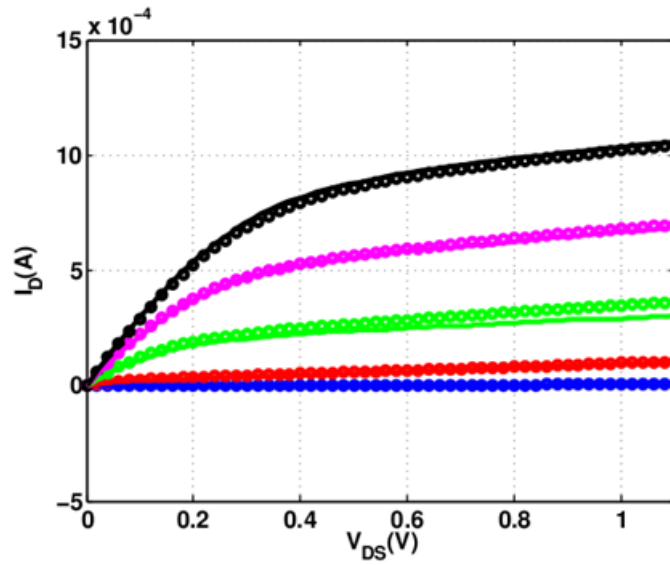


Figure 2.35:  $I_{DS} - V_{DS}$  curve linear scale fitting result with multiple biases using  $\tau = 0.007ps$ ,  $V_{sat} = 1.3e7cm/s$ .

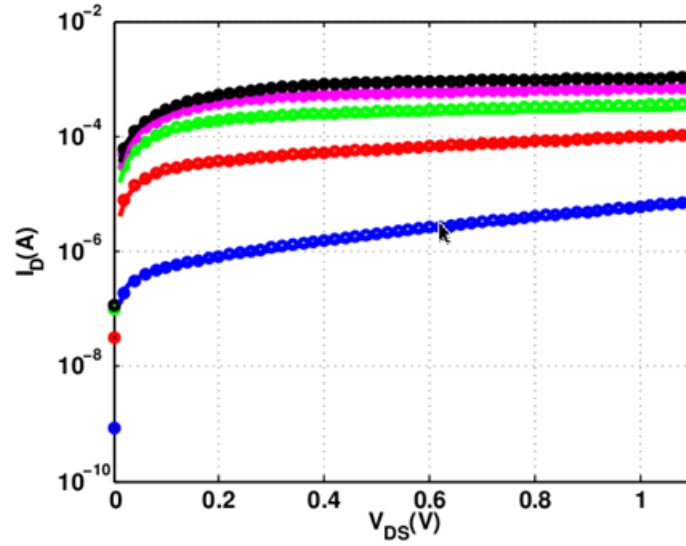


Figure 2.36:  $I_{DS} - V_{DS}$  curve log scale fitting result with multiple biases using  $\tau = 0.007ps$ ,  $V_{sat} = 1.3e7cm/s$ .

## 2.7 Conclusion

It is apparent that both  $I_{DS} - V_{GS}$  and  $I_{DS} - V_{GS}$  simulation curves with multiple biases can match the measurement data curves. Since from the result it can be conclude that among the two groups of calibrated saturation velocity and relaxation time, the second group can match the curves better. So the second group of parameter values should be applied. DC I-V character calibration is finished. Next step is to start noise simulation and analysis.

## Chapter 3

### Noise Simulation and Interpretation

MOSFET RF noise has been studied these years, mainly from  $40nm$  to  $200nm$  gate length devices. However with the channel length continuously shrinking, noise parameter increase significantly in high  $V_{DS}$ . With TCAD, noise can be simulated inner physical mechanism of MOSFETs. This chapter presents the simulation process and result of the noise feature.

#### 3.1 TCAD noise simulation

Sentaurus Device treats noise analysis, fluctuation analysis and sensitivity analysis by the impedance field method, and as extension of small-signal analysis. For noise and random fluctuations, Sentaurus Device computes the variances and correlation coefficients for the voltages at selected circuit nodes, assuming the net current to these nodes is fixed. As the computation is performed in frequency space, the computed quantities are called noise voltage spectral densities. Sentaurus Device also computes the variances and correlation coefficients of the currents through the nodes assuming fixed voltages; these quantities are the noise current spectral densities. There are several noise sources in Sentaurus Device: Diffusion Noise, Equivalent Monopolar Generation-Recombination Noise, Bulk Flicker Noise, Trapping Noise, Random Dopant Fluctuations Random Geometric Fluctuations and other kinds of fluctuations[18].

#### 3.2 DD and HD Model for Noise simulation

Transport models have significant impact on thermal noise. DD model and HD transport model are two common transport models used in Sentaurus Device simulation process.

Firstly, brief introduction for these two transport models will be given. DD model is the abbreviation of Drift-Diffusion model, which is the most commonly used transport model and the default transport model in Sentaurus Device simulation. Poisson equation and Continuity equation are the governing equations for charge transport in semiconductor device. Poisson equation and continuity equation is given by:

$$\Delta \cdot \epsilon \nabla \phi = -q(p - n + N_D - N_A) - \rho_{trap}, \quad (3.1)$$

$$\nabla \cdot \vec{J}_n = qR_{net} + q\frac{\partial n}{\partial t}, \quad (3.2)$$

$$\nabla \cdot \vec{J}_p = qR_{net} + q\frac{\partial p}{\partial t}, \quad (3.3)$$

where  $\epsilon$  is the electrical permittivity;  $n$  and  $p$  are the electron and hole densities;  $q$  is the elementary electron charge;  $N_D$  and  $N_A$  are concentrations of ionized donors and acceptors.  $\rho$  is the charge density contributed by traps and fixed charges.  $R_{net}$  is the net electron and hole recombination rate.  $\vec{J}_n$  and  $\vec{J}_p$  are electron and hole current density. So for drift-diffusion model, the current density for electrons and holes are given by:

$$\vec{J}_n = \mu_n(n\nabla Ec - 1.5nkT\nabla \ln m_n) + D_n(\nabla n - n\nabla \ln \gamma_n), \quad (3.4)$$

$$\vec{J}_p = \mu_p(p\nabla Ev - 1.5pkT\nabla \ln m_p) + D_p(\nabla p - p\nabla \ln \gamma_p), \quad (3.5)$$

The first term takes into account the contribution due to the spatial variations of the electrostatic potential, the electron affinity and the band gap.  $m_p$  and  $m_n$  are effective masses for electrons and holes.

HD model is the abbreviation of Hydrodynamic model. Hydrodynamic model accounts for energy transport of the carriers, which is suitable for devices with small active region. 28nm gate length MOSFETs have small active regions, hydrodynamic model should be used

in Sentaurus Device simulations especially for thermal noise simulation. The current density of hydrodynamic model of electrons and holes are defined as:

$$\vec{J}_n = \mu_n(n\nabla Ec + kT_n\nabla n - nkT_n\nabla \ln \gamma_n + \lambda_n kn \int_n^{td} \nabla T_n - 1.5nkT\nabla \ln m_n) \quad (3.6)$$

$$\vec{J}_p = \mu_p(p\nabla Ev + kT_p\nabla p - pkT_p\nabla \ln \gamma_p + \lambda_p kp \int_p^{td} \nabla T_p - 1.5pkT\nabla \ln m_p) \quad (3.7)$$

### 3.3 Impedance Field Method in TCAD Simulation

The impedance field method splits noise and fluctuation analysis into two tasks. The first task is to provide models for the noise sources, that is the local microscope fluctuations inside the devices. The second task is to determine the impact of the local fluctuations on the terminal characteristics. In order to solve this task, Green functions are used on each contact. These green functions are completely specified by the transport model, which is hydrodynamic in this research. Then after each numeric calculation, the output can be obtained. The noise simulation output data can be generated using NoisePlot command. LNS abbreviation of local noise source and LNVSD local current voltage spectral density also can be called noise concentration are the key variables. Thus, plots are generated using simulated data, and the bias conditions are  $V_{GS} = 0.6V$ , and  $V_{DS} = 0.6V$ :

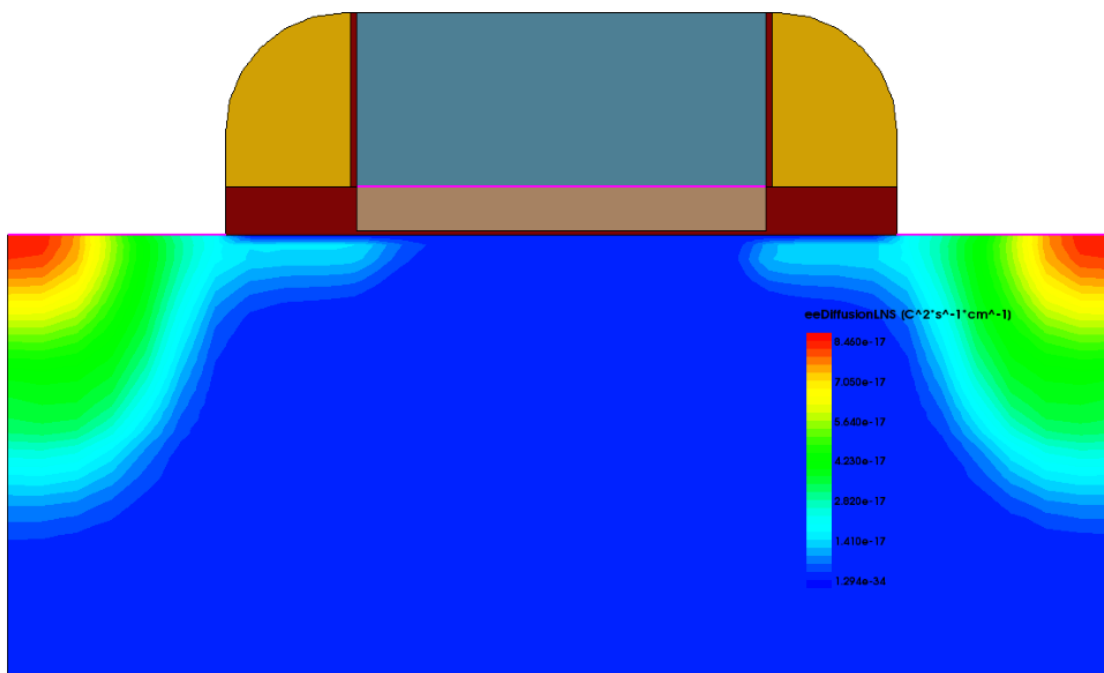


Figure 3.1: Local noise source distribution in device at  $f = 10GHz$ ,  $V_{DS} = 0.6V$ ,  $V_{GS} = 0.6V$ .

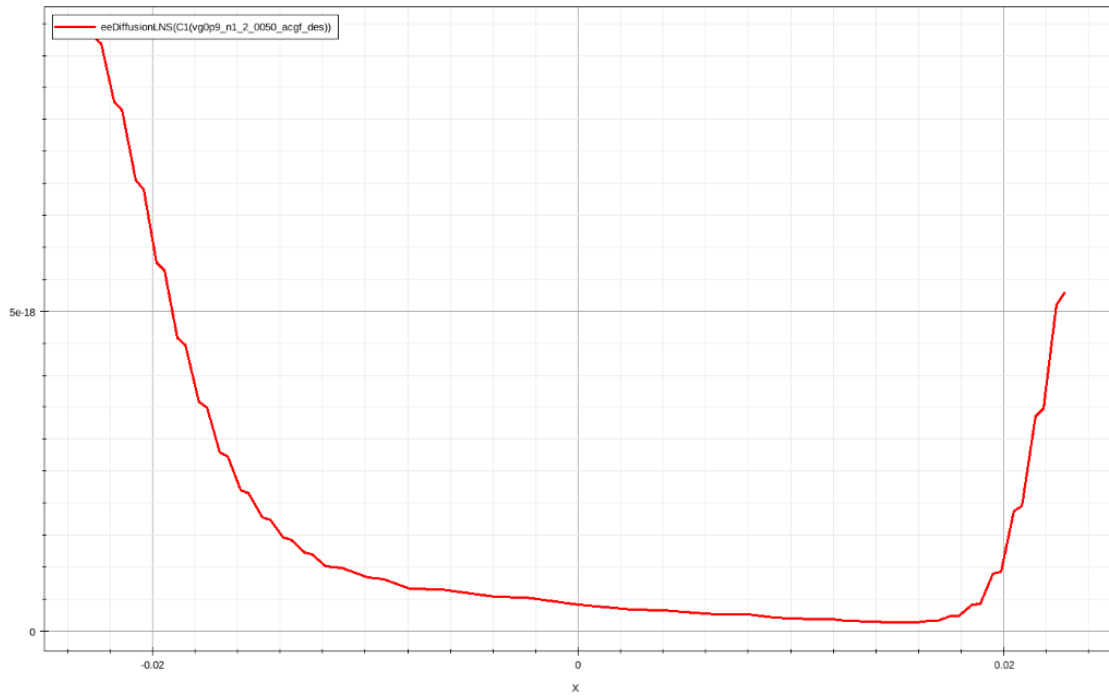


Figure 3.2: Local noise source simulated cut data at  $f = 10GHz$ ,  $V_{DS} = 0.6V$ ,  $V_{GS} = 0.6V$ .

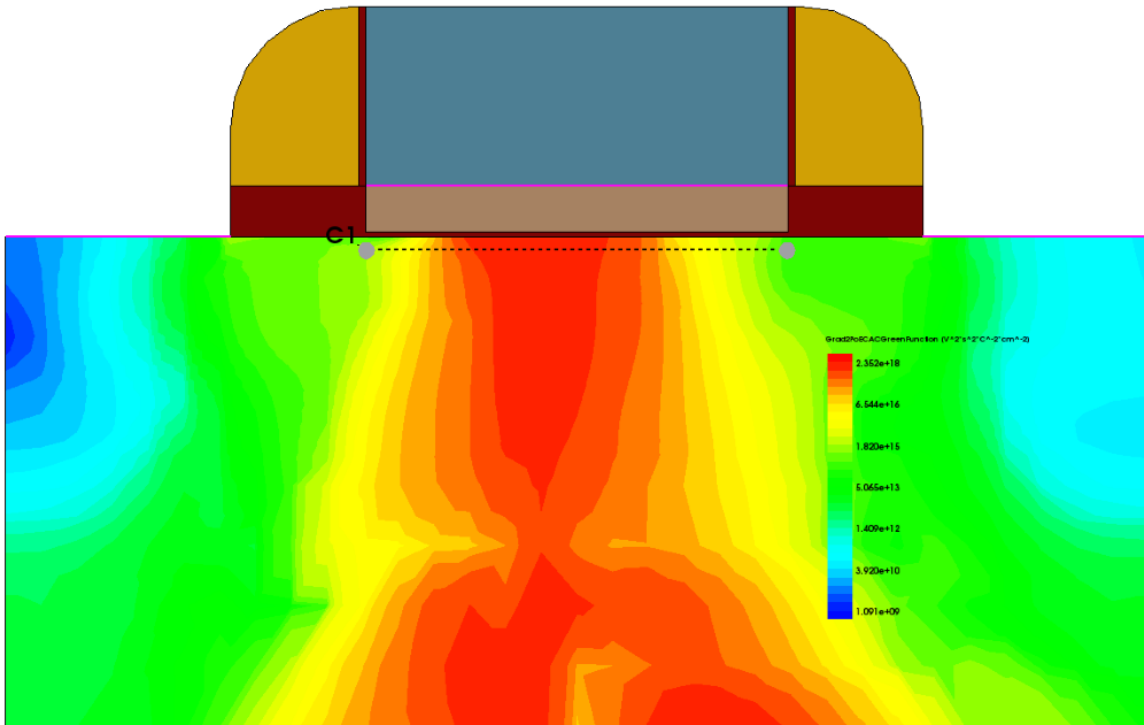


Figure 3.3: Green function  $f = 10GHz$ ,  $V_{DS} = 0.6V$ ,  $V_{GS} = 0.6V$ .

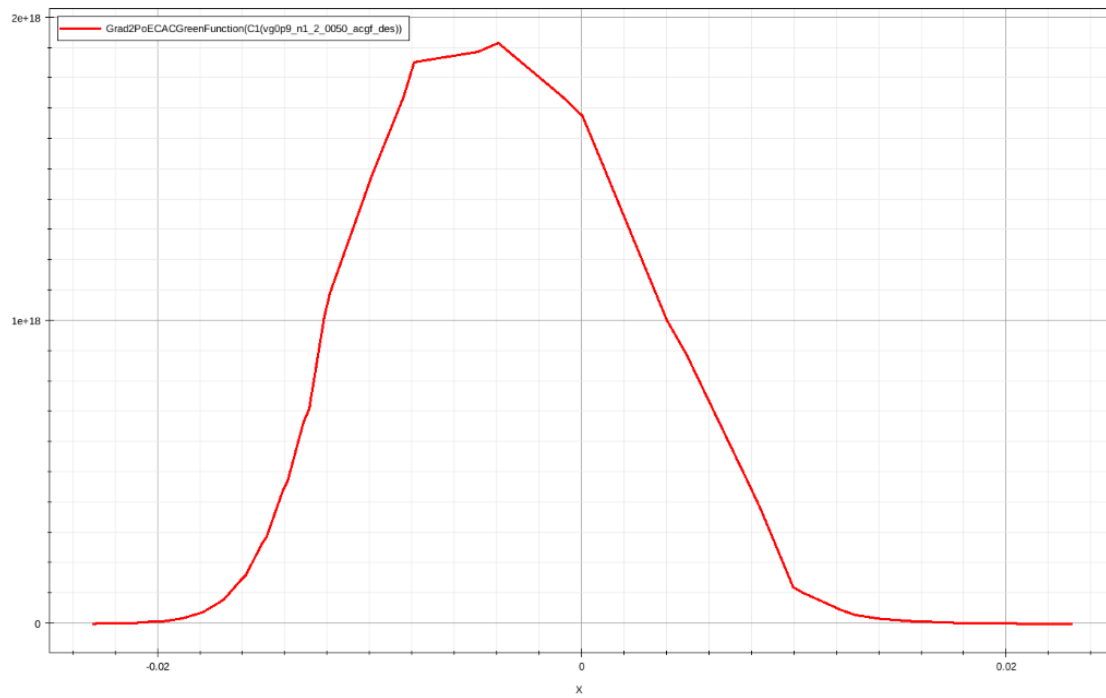


Figure 3.4: Vector Green's function simulated data at  $f = 10GHz$ ,  $V_{DS} = 0.6V$ ,  $V_{GS} = 0.6V$ .

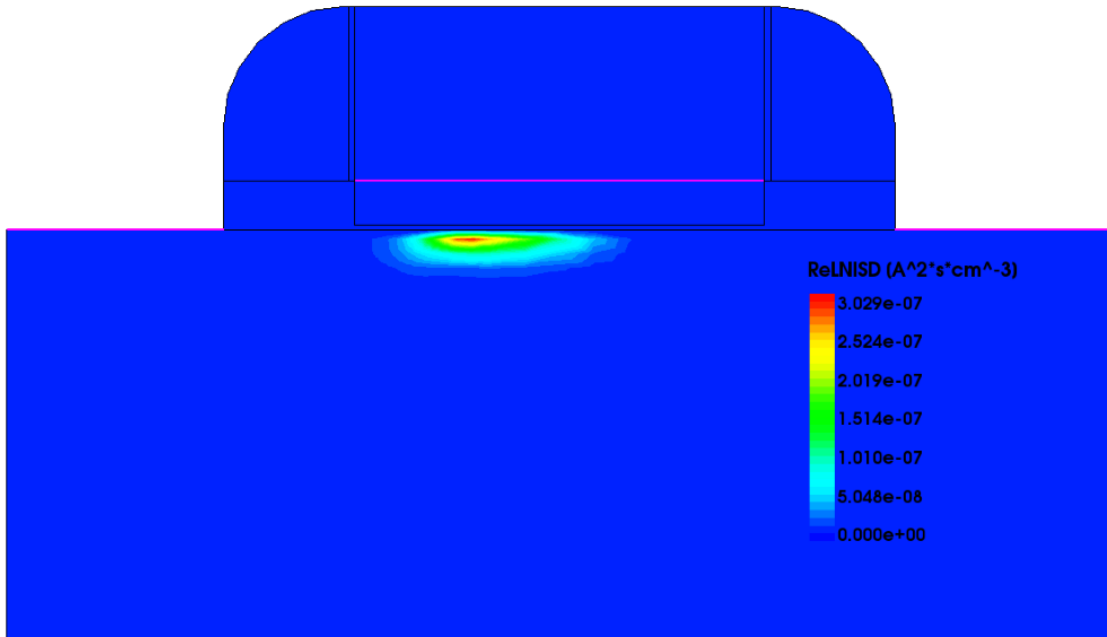


Figure 3.5: Local noise current spectral density distribution at  $f = 10GHz$ ,  $V_{DS} = 0.6V$ ,  $V_{GS} = 0.6V$ .

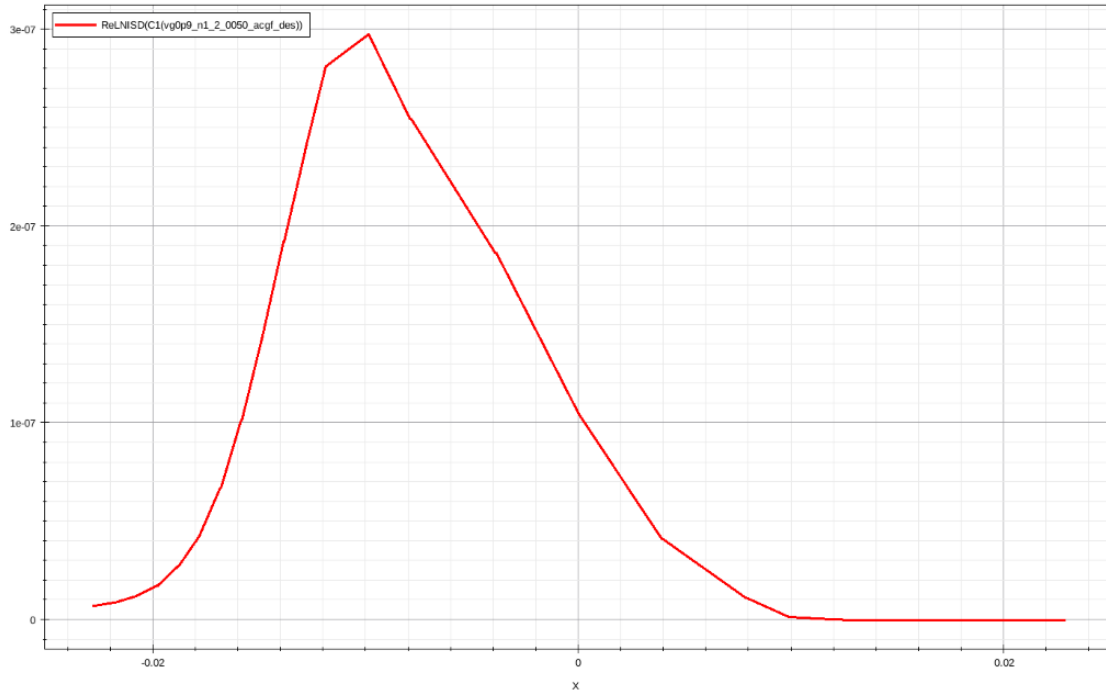


Figure 3.6: Local noise current spectral density simulated data at  $f = 10GHz$ ,  $V_{DS} = 0.6V$ ,  $V_{GS} = 0.6V$ .

### 3.4 Noise Simulation Result and Analysis

After successful calibration of the  $28nm$  gate length MOSFETs device, noise parameter can be simulated using calibrated mobility model parameters. Besides, hydrodynamic transport model is applied in noise simulation. Different  $V_{GS}$  biases for noise simulation:  $0.3V$  and  $1.1V$  are applied.  $\gamma$  verses  $V_{DS}$  curve is plotted out for result analysis and the results are shown as:

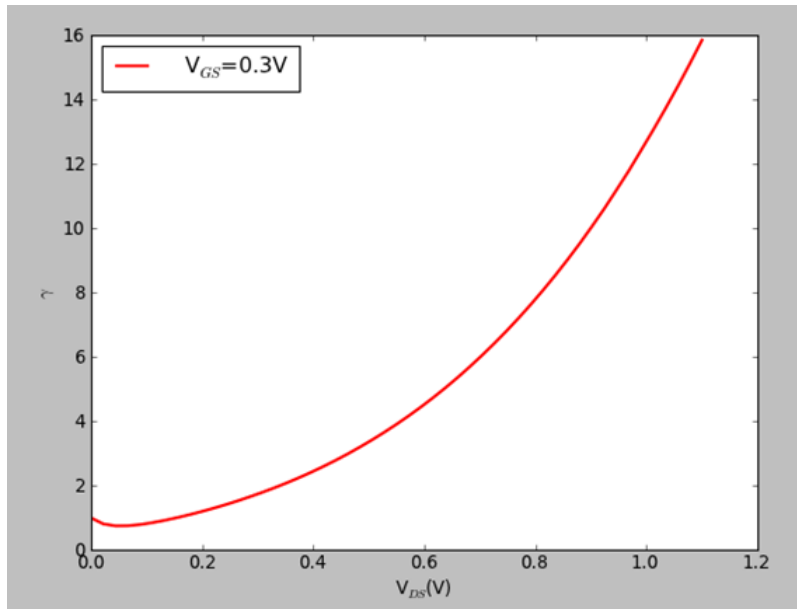


Figure 3.7: Simulated  $\gamma_{gd0}$  versus  $V_{DS}$  at  $V_{GS} = 0.3V$ .

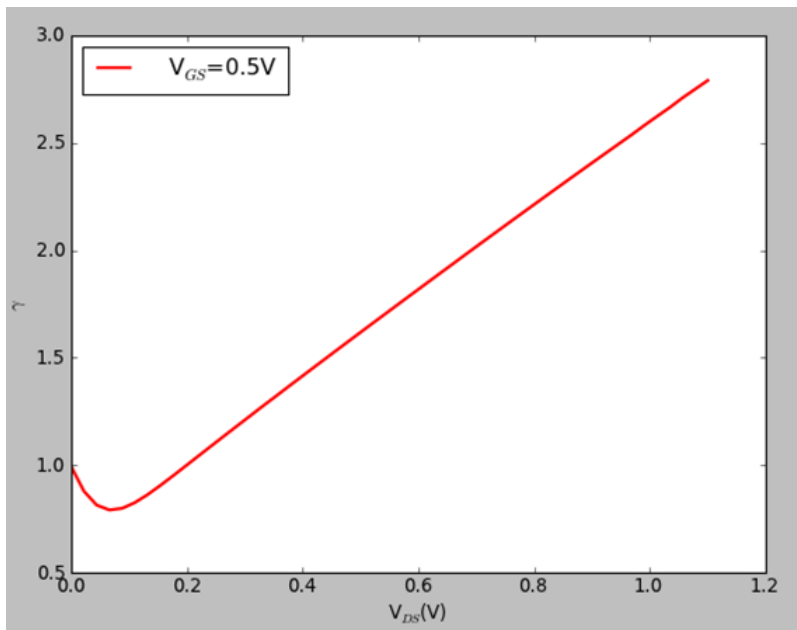


Figure 3.8: Simulated  $\gamma_{gd0}$  versus  $V_{DS}$  at  $V_{GS} = 0.5V$ .

From the simulation results, it can be observed that with the gate voltage increase, the noise parameter  $\gamma$  decreases and then increase at different  $V_{DS}$  point at different gate bias conditions. For gate voltage equal to  $0.3V$ , the noise parameter increase continuously along with the increment of  $V_{DS}$ ; For gate voltage equal to  $0.5V$ , the noise parameter rise back up after  $V_{DS}$  is larger than  $0.2V$ . For gate voltages larger than  $0.5V$ , the noise parameter curve change point also move towards positive direction. However, overall, the noise parameter  $\gamma$  decrease with the the increase of gate bias. However, the simulation result curves at high  $V_{GS}$  are not smooth.

### 3.5 Noise simulation and measurement data comparison

The noise measurement data is conduct under gate bias, The relaxation time used is  $0.02ps$  and saturation velocity is  $1.2 \times 10^7 cm/s$ . The two points on the Figure 3.9 are the measurement data at  $V_{GS} = 0.6V, f = 10GHz$ . Noise measurement data has two values at  $V_{DS} = 0.4V$  and  $V_{DS} = 0.8V$  under  $V_{GS} = 0.6V$  bias. So after simulation, the comparison result is shown in Figure 3.12:

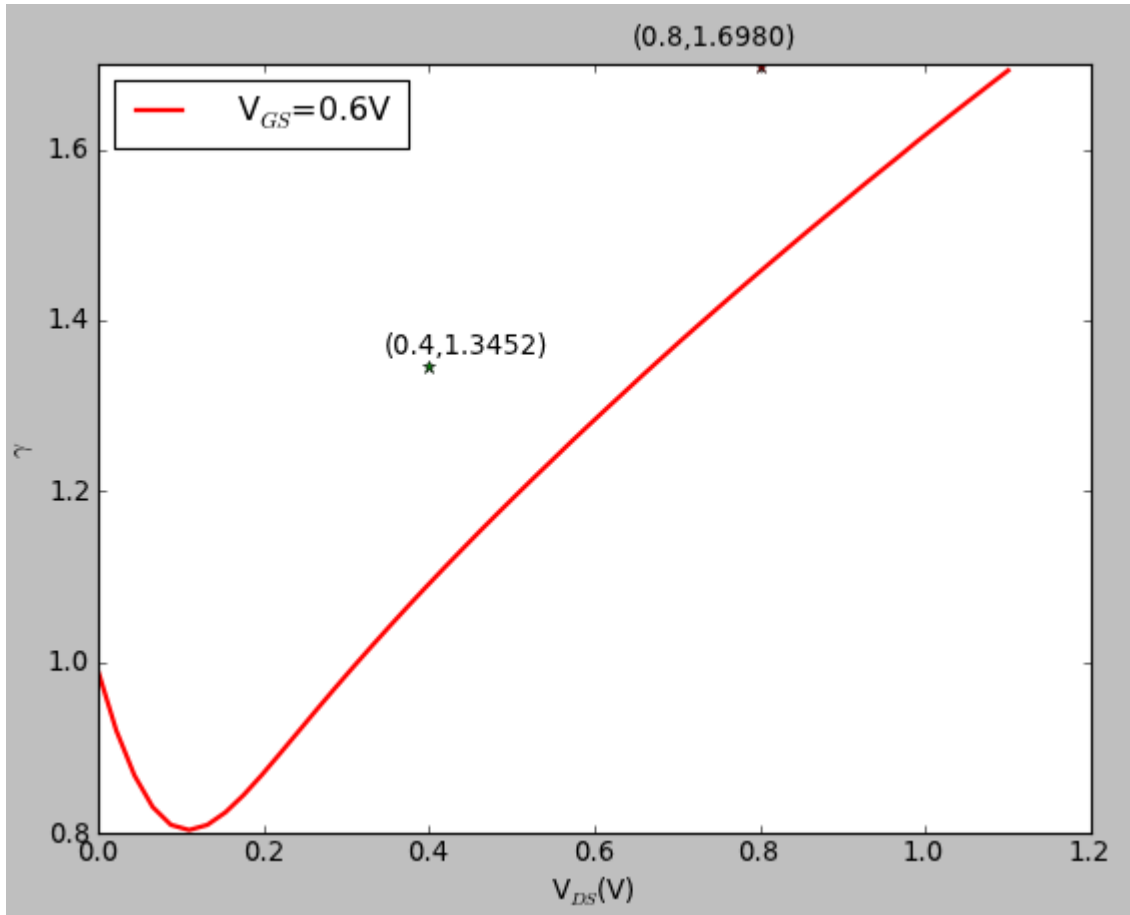


Figure 3.9: Noise simulation and measurement comparison  $\tau = 0.02ps$ ,  $V_{sat} = 1.2 \times 10^7 cm/s$ .

The two points in the figure represents the measurement data at  $V_{DS} = 0.4V$ ,  $V_{DS} = 0.8V$ . We can see there are some difference between the measurement data and simulated data, but it is close.

## Chapter 4

### Conclusion and Future Work

A  $28nm$  gate length MOSFETs device is built and calibrated in this thesis, and noise simulation process and results are presented. After capacitance,  $I - V$  characteristics and mobility calibration, the simulated curves and measurement curves are compared. The simulated data and measurement data can match well after all calibration steps. By using impedance field method the noise parameter is calculated and compared to measurement data. And the simulated noise data is close to measurement data. But the simulated noise curves under high  $V_{GS}$  bias conditions are not smooth. This is caused by discontinuity in mobility model parameters which need to be modified in the future. Also there are analysis and discussions on mobility parameter impact on RF noise.

## Bibliography

- [1] Tsividis. Y, "Operation and Modeling of the MOS Transistor", 2nd edn. McGraw Hill, New York, 1999
- [2] A.Van der Ziel, "Thermal noise in field effect transistor", Proc. IRE, vol.50, pp.1808-1812, Aug 1962.
- [3] A.Van der Ziel, *Noise in solid-State Devices and Circuit*, John Wiley Sons, 1986.
- [4] A.J.Scholten, L.F. Tiemeijer, R.J.Havens, R.de Kort, R. wan Langevelde, and D.B.M.Klaassen, "RF noise modeling and characterization", *2006 IEEE MTT-S International Microwave Symposium*, 2006.
- [5] Yan Cui, "High Frequency Noise Modeling and Microscopic Noise Simulation for SiGe HBT and RF CMOS", 2005
- [6] *DESSIS, 2-D Device Simulator, version 9.0*. Synopsys.
- [7] Jindal, R.P. Internal technical memorandum. ATT Bell Laboratories, Murray Hill, NJ, 1984
- [8] Jindal, R.P, "Hot electron effects on channel thermal noise in fine line NMOS field effect transistors". *IEEE Trans. Electron Devices* 33(9),1395-1397, 1986
- [9] Jindal, R.P, "From millibits to terabits and beyondover 60 years of innovation". *Invited paper, In: Proc. 2nd IEEE Int. Workshop on Elect. Devices and semicond. Tech.*, Mumbai, India, 2009
- [10] Jindal, R.P. "High frequency noise in fine line NMOS field effect transistors". in *IEDM Tech.Dig.*, pp.68-71 (1985)(invited paper)
- [11] Chen C.-H, Deen, M.J, "Channel noise modeling of deep submicron MOSFETs". *IEEE Tans. Electron Devices* February 2014
- [12] R.P. Jindal, H. Shichijo, S. Martin, F.C. Hon, C. Machala, and D.E. Trombley, "A physical understanding of RF noise in bulk nMOSFETs with channel lengths", *IEEE Transaction on Electron Devices*, vol.59, no.1, pp.197-205, 2012
- [13] *TAURUS, 2-D Device Simulator*, Synopsys.
- [14] *TAURUS, Process Simulator*, Synopsys.

- [15] Yannis Tsividis and Colin McAndrew “THE MOS TRANSISTOR”, *Oxford University Press Inc. 2011.*
- [16] Yannis Tsividis and Colin McAndrew “THE MOS TRANSISTOR INTERNATIONAL THRID EDITION” chapter ”Small-Channel and Thin Oxide Effects”, *Oxford University Press Inc.*
- [17] *Sentaurus Device User Guide*, version G2012.06, June 2012. Synopsys.
- [18] Jindal, R.P, “Noise phenomena in submicron channel length silicon NMOS transistors” in *8th Int. Conf. Noise Phys. Syst. 4th Int. Conf, Rome, Italy*, pp.199-202(1985)